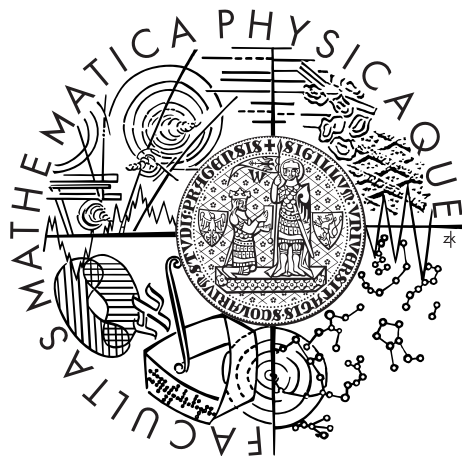


Charles University in Prague  
Faculty of Mathematics and Physics

## MASTER THESIS



Martin Pecka

# Detection of 2D features in MARSIS ionogram pictures

Department of Software Engineering

Supervisor of the master thesis: RNDr. Jana Štanclová, Ph.D.

Study programme: Informatics

Specialization: Theoretical Informatics

Prague 2013

Dedication.

I declare that I carried out this master thesis independently, and only with the cited sources, literature and other professional sources.

I understand that my work relates to the rights and obligations under the Act No. 121/2000 Coll., the Copyright Act, as amended, in particular the fact that the Charles University in Prague has the right to conclude a license agreement on the use of this work as a school work pursuant to Section 60 paragraph 1 of the Copyright Act.

In Prague date .....

Název práce: Hledání 2D jevů v ionografických snímcích přístroje MARSIS

Autor: Bc. Martin Pecka

Katedra: Katedra softwarového inženýrství

Vedoucí diplomové práce: RNDr. Jana Štanclová, Ph.D.,  
Ústav výpočetní techniky Univerzity Karlovy v Praze

**Abstrakt:** Práce se zabývá technikami hledání význačných prvků v ionogramech zachycených přístrojem MARSIS umístěným na kosmické sondě Mars Express. Identifikace těchto prvků pomáhá při studiu ionosféry, magnetosféry a plazmatu v okolí Marsu. Ionogramy jsou reprezentovány jako dvourozměrné obrázky s hodnotou kódovanou pomocí barvy. Cílem práce je navrhnout techniky pro detekci různých zajímavých křivek (definovaných sadou parametrů) v ionogramech, případně pro měření dalších parametrů nalezených objektů (perioda opakování přímek).

**Klíčová slova:** rozpoznávání vzorů, detekce objektů, parametrické křivky, Mars Express, vektorizace

Title: Detection of 2D features in MARSIS ionogram pictures

Author: Bc. Martin Pecka

Department: Department of Software Engineering

Supervisor: RNDr. Jana Štanclová, Ph.D., Charles University Computer Centre

**Abstract:** The work focuses on techniques for finding significant features in ionograms captured by the MARSIS instrument onboard the Mars Express spacecraft. Identification of these features helps in studying the ionosphere, magnetosphere and plasma surrounding Mars. Ionograms are 2D images with values represented in color. The goal of this work is to propose techniques to detect interesting curves (parametrically defined) in such images and to measure some more parameters of the found objects (like the repetition period of lines).

**Keywords:** pattern recognition, object detection, parametric curves, Mars Express, vectorization

# Contents

<b>Introduction</b>	<b>3</b>
<b>1 Mars Express, MARSIS and ionograms</b>	<b>5</b>
1.1 Mars Express . . . . .	5
1.1.1 High-Resolution Stereo Camera (HRSC) . . . . .	6
1.1.2 Observatoire pour la Minéralogie, l'Eau, les Glaces et l'Activité (OMEGA) . . . . .	8
1.1.3 Mars Advanced Radar for Subsurface and Ionosphere Sounding (MARSIS) . . . . .	8
1.1.4 Planetary Fourier Spectrometer (PFS) . . . . .	9
1.1.5 SPectroscopy for the Investigation of the Characteristics of the Atmosphere of Mars (SPICAM) . . . . .	10
1.1.6 Analyser of Space Plasmas and EneRgetic Atoms (ASPERA-3) . . . . .	11
1.1.7 Mars Express Orbiter Radio Science (MaRS) . . . . .	12
1.1.8 Beagle 2 . . . . .	13
1.2 The MARSIS experiment . . . . .	14
1.2.1 Subsurface sounding . . . . .	14
1.2.2 Surface sounding . . . . .	15
1.2.3 Ionospheric sounding . . . . .	15
1.3 Ionograms . . . . .	16
1.3.1 Ionospheric echo . . . . .	17
1.3.2 Surface echo . . . . .	18
1.3.3 Oblique ionospheric echo . . . . .	18
1.3.4 Electron plasma oscillation harmonics . . . . .	20
1.3.5 Electron cyclotron echoes . . . . .	20
<b>2 The detection problem</b>	<b>22</b>
2.1 Definitions . . . . .	22
2.1.1 Definition of ionogram . . . . .	22
2.1.2 Specification of the features to detect . . . . .	24
2.1.3 Specification of the detection results . . . . .	26
2.1.4 Definition of the detection problem . . . . .	27
2.2 Data formats . . . . .	28
2.2.1 Data source . . . . .	28
2.2.2 Input files format . . . . .	28
2.2.3 Output files format . . . . .	29
2.3 Automated detection . . . . .	29

2.3.1	Current ways of solving the problem . . . . .	30
2.3.2	Proposed solutions . . . . .	31
<b>3</b>	<b>Lateral histograms</b>	<b>33</b>
3.1	Lateral histograms applied to ionograms . . . . .	33
3.1.1	Definition . . . . .	33
3.1.2	Simplification in the case of ionograms . . . . .	33
3.2	Implementation . . . . .	35
3.2.1	Finding and filtering the peaks . . . . .	35
3.2.2	Using the peaks of row/column sums . . . . .	35
3.3	Period estimation . . . . .	37
3.3.1	Periodograms . . . . .	37
3.3.2	Sine wave least squares fitting . . . . .	40
3.3.3	Period averaging . . . . .	43
3.3.4	Combining the methods . . . . .	44
3.4	Vertical periods detection . . . . .	46
3.5	Ground echo detection . . . . .	46
3.6	Summary of lateral histogram methods . . . . .	47
<b>Conclusion</b>		<b>49</b>
<b>Appendix 1</b>		<b>50</b>
<b>Bibliography</b>		<b>51</b>
<b>List of Tables</b>		<b>56</b>
<b>List of Abbreviations</b>		<b>57</b>
<b>Attachments</b>		<b>58</b>

# Introduction

Space exploration in its wider meaning has accompanied the mankind almost as long as e.g. writing. Looking at the stars, connecting them into constellations and thinking about the nature of the stars and the space between them – all activities have been of interest for many people.

Up until the 50's of the 20<sup>th</sup> century, these observations were limited to remote study. Telescopes (and very, very later spectrometers, too) were the only ways of getting some useful information about cosmic bodies. Not a small number of information can be deduced from these observations, but sure there are many of them needing either better resolution unreachable from the Earth or requiring in situ measurements. To name some of the remotely observable properties, we can mention e.g. orbit measurements, mass estimates, gravity effect observations, overall chemical make-up determination (through spectroscopy) or deep-space radio waves analysis. With the development of technology many new procedures were engineered for measuring many other parameters of the cosmic bodies.

Starting with the successful launch of Sputnik 1, the first Earth's artificial satellite, the mankind entered the new epoch of in situ space exploration. Many space crafts have been launched since then with the most varied purposes and heading to all reachable interesting destinations in our Solar system (or staying at Earth's orbit). Some of them, like the Voyager 1 or Pioneer 10 are even heading out of the Solar system to explore the outer space.

After exploring the Moon (the NASA's Apollo missions) and Venus (USSR's Venera and Vega and NASA's Mariner, Magellan and Pioneer-Venus missions), the third nearest space neighbor of Earth was to be explored from close range – Mars. Missions like Viking, Mars Global Surveyor, Mariner, Mars Odyssey or Fobos had Mars as their destination and target of observation.

In 2003 the European Space Agency (ESA) launched its orbital planetary explorer called Mars Express (MEX). Its primary target has been to detect traces of life on the planet, which became a very popular problem in the 21<sup>st</sup> century. Although its primary mission ended in 2005, the probe has still (as of 2013) continued in operation and has been sending more and more scientific data to the Earth. Besides photos of the surface served in unrivaled resolution, it also proved presence of water and methane on Mars and in total has brought a lot of important scientific discoveries.

In our thesis we focus on one specific equipment of MEX – the MARSIS radar. It is used for ionosphere and subsurface sounding using long radio waves. This is a technique allowing to detect subsurface structures as well as to determine the density profiles of the ionosphere. Using the subsurface sounding mode, MARSIS confirmed the existence of water ice under the surface. In particular, of our

interest is the ionospheric sounding mode and the data it produces.

The ionospheric sounding data are received in the form of so called “ionograms” which can be imagined as two-dimensional images with intensity-coded data. In these images, several types of linear features are to be detected in order to extract the measured physical properties of ionosphere and plasma.

All these features have been extracted manually up to the present, which is on one hand very reliable, but on the other hand time-consuming and boring. The goal of our work is to examine several computer vision methods on this problem and try to find some performing the detection automatically as well as reliably. We aim at a conducting a comparative test of these methods and telling the pros and cons of each of them.

In Chapter 1 we describe the Mars Express orbiter in detail along with all its onboard experimental appliances. Chapter 2 defines the solved task precisely and analyses the ionograms and the general properties of the studied features. The subsequent chapters are then each dedicated to a different method of solving the task. In the last chapter we provide a short summary of the presented techniques as well as their comparison and analysis of the obtained results.

# 1 Mars Express, MARSIS and ionograms

In this chapter we introduce the Mars Express spacecraft and its scientific payload. We describe all the appliances, their goals and successes so far. In the second section we present the MARSIS instrument in detail showing the principles of its experiments. The last part of this chapter is devoted to the description of ionograms – a specific visualization of the ionospheric sounding data from MARSIS.

## 1.1 Mars Express

First of all, we briefly introduce the spacecraft carrying all the equipment needed to acquire ionograms. Its name is Mars Express (MEX) and it was launched by the European Space Agency (ESA) on June 2, 2003. A visualization of the spacecraft is provided in Figure 1.1.

MEX arrived to Mars at its orbit with periapsis 250 km and apoapsis over 11,000 km on December 25, 2003 [15] with seven onboard scientific instruments and a landing module called Beagle 2. Unfortunately, the landing sequence of Beagle 2 failed (for an unknown reason) and the lander did not establish connection after it landed (if it landed at all)[15, p. 4].

The mission of MEX has several goals like “global studies of the surface, subsurface and atmosphere at unprecedented spatial and spectral resolutions” [15, p. viii]. One of the goals, however, stands out among all the others. It is the search for water (or its traces) on martian surface or subsurface.

There is lots of geological evidence of former water occurrence on Mars [15, p. ix]. But before the MEX mission nobody had proved or refuted presence of water on Mars in the present. Knowing more about water on Mars and its history, the scientists could postulate better hypotheses about the possibility of (former) life on the planet [15, p. ix].

The original mission lifetime of MEX was projected up to the end of 2005 (which would be 1 Martian year = 687 Earth days) [16]. During its lifetime, MEX encountered some small problems<sup>1</sup>. Nevertheless, it has worked on its science goals up to this day and its science mission was extended until 2014 [22] (after 3 preceding similar extensions). According to Fred Jansen, MEX mission manager, MEX had enough fuel for another 14 years of operation (at the beginning of 2012) [11]. So there is a hopeful prospect of further and even

---

<sup>1</sup>as the Solid State Mass Memory anomalies described in [20] or the MARSIS antennas deployment problems in 2004 [17, 18]

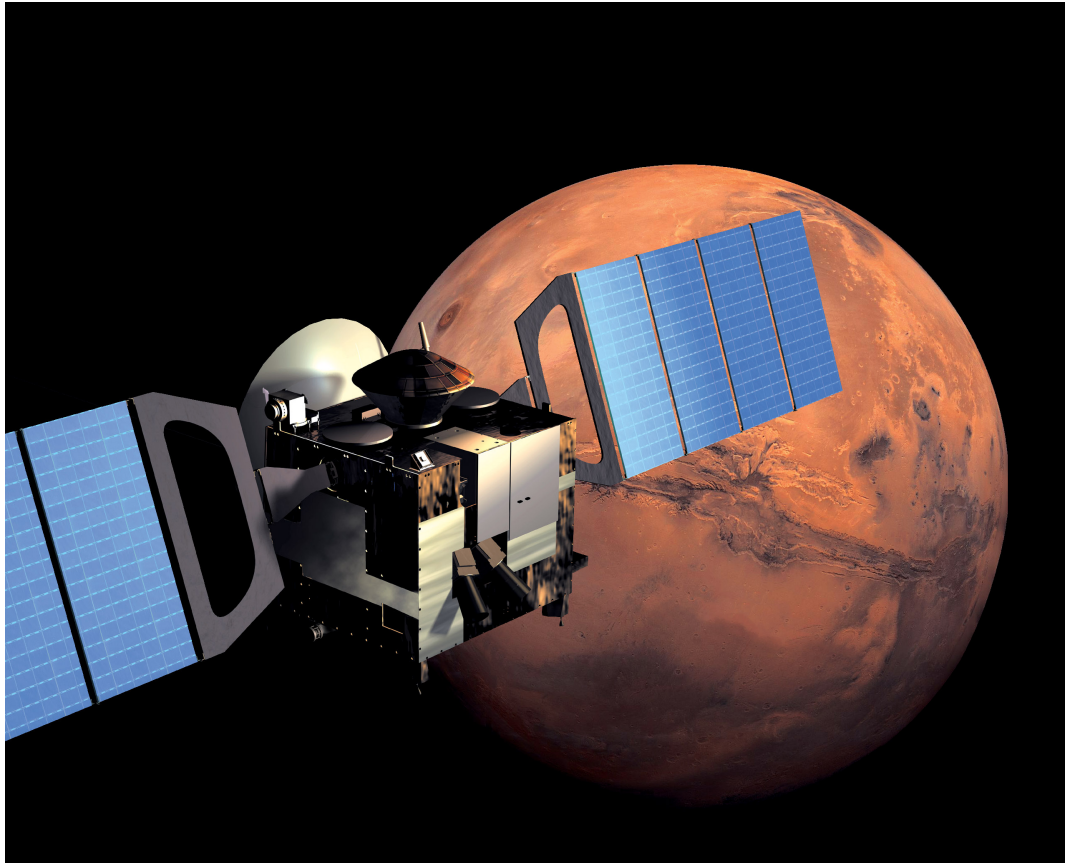


Figure 1.1: Mars Express spacecraft. [19]

deeper Mars exploration (e.g. like the discovery of an unexpected way of using the MARSIS instrument which “added magnetometer functionality” to MARSIS [24]).

In the next subsections particular MEX instruments are described. The descriptions are based on [15] which can be consulted for more detailed information.

### 1.1.1 High-Resolution Stereo Camera (HRSC)

HRSC is a high-resolution pushbroom<sup>2</sup> camera for surface imaging. Its goals are [15, p. 17]:

- to characterize surface structure and morphology at resolution  $10 \text{ m.px}^{-1}$  (regions of interest at  $2 \text{ m.px}^{-1}$ ),
- to record surface topology at high vertical resolution,
- to observe atmospheric phenomena,
- to analyze physical properties of the surface,

---

<sup>2</sup>A camera that scans the image by rows perpendicular to the flight direction. See [http://earthobservatory.nasa.gov/Features/E01/e01\\_2.php](http://earthobservatory.nasa.gov/Features/E01/e01_2.php) for more details.

- to classify terrain and thus refine the martian cartographic base,
- to observe martian moons Phobos and Deimos during their approaches.

HRSC is able to capture the surface at resolution up to  $10 \text{ m.px}^{-1}$  with field of view  $11.9^\circ$ , covering a 52.2 km wide strip of surface at height 250 km (which is the periapsis of MEX). The camera consists of 9 CCD (Charge-coupled device) sensors allowing it to acquire triple stereo images in 4 colors and 5 phase angles. A very useful property of these images is that they are taken nearly simultaneously and thus have the same illumination and other observational conditions (which further helps in photogrammetric processing of the images) [15, pp. 24–30].

In addition to the stereo camera, the instrument also contains a super-high-resolution camera called SRC (Super-Resolution Channel) aimed at targeted observations of particular surface details. With image resolution  $2.3 \text{ m.px}^{-1}$  and field of view  $0.54^\circ$  it provides a detailed view of a  $2.3 \times 2.35 \text{ km}$  large surface. Its main purpose is to take details of places of interest, e.g. future landing sites for other landing modules [15, p. 28].

Up to November 2011 HRSC had covered about 88 % of the martian surface [21, pp. 72–73] and still continues to gather new data. An example photograph from HRSC is given in Figure 1.2. The scientific results of HRSC are for example:

- better exploration of fluvial valleys [30],
- discovery of numerous glacial landforms [23, p. 5],
- investigating lava flows [23, p. 28],
- discovery of “dust devils” (fast moving dust storms) [23, p. 47],
- providing data to derive a detailed topographic model of more than 20 % of Phobos [25, pp. 945–949].

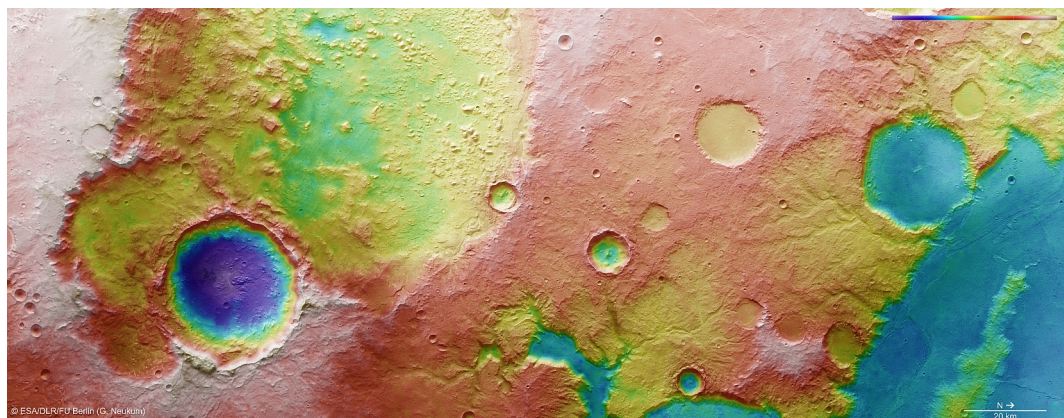


Figure 1.2: Example image taken by HRSC. [34]

### **1.1.2 Observatoire pour la Minéralogie, l'Eau, les Glaces et l'Activité (OMEGA)**

OMEGA is a medium- and high-resolution spectrometer operating in visible and near-infrared (near-IR) spectra ( $0.38\text{--}5.1\,\mu\text{m}$  wavelength). Its medium-resolution operating mode (from heights of 1,500 to 4,000 km) can measure with the resolution 2–5 km targeting at global surface coverage. In the high-resolution mode (from the close vicinity of periapsis) it achieves resolution 350 m or better, but can cover only a small fraction of the surface [15, p. 37].

As stated in [15, pp. 38–39], the main goals of OMEGA are:

- to study the evolution of Mars,
- to detect minerals hidden to lower resolutions,
- to map mineralogical boundaries between geological units,
- to reveal gradients in hydration minerals related to fossil water flows,
- to monitor features associated with wind transportation.

In particular, OMEGA is intended to find carbonates (not found on martian surface until the launch of MEX) and water ice. It is also able to measure atmospheric pressure, CO and H<sub>2</sub>O column densities and surface temperature.

Recent contributions of the OMEGA payload are e.g.:

- confirmation of liquid water on the surface when the planet was young [28],
- discovery of IR and ultraviolet (UV) glows in the atmosphere [6],
- proving that Mars had a hot and wet period [9] (implying there were lots of greenhouse gases and a strong magnetic field, too [23, p. 90]),
- analyzing the south polar cap and finding out it is formed mainly of water ice [13],
- observation of CO<sub>2</sub> ice clouds [33],
- finding ferric oxides near the equator [32].

### **1.1.3 Mars Advanced Radar for Subsurface and Ionosphere Sounding (MARSIS)**

MARSIS is a long-wavelength radar using coherent wide-band pulses for sounding of the surface, subsurface and ionosphere of Mars. For these purposes it uses a 40 m dipole antenna (for both transmitting and receiving) and a shorter 7 m

monopole antenna (only for receiving). Due to the used sounding frequencies ranging from 100 kHz to 5.5 MHz it is able to reach the depth about 5–8 km under the surface [15, pp. 51, 57].

The primary goal of MARSIS is to detect liquid and solid water in the upper crust of Mars. There are also other objectives [15, p. 51]:

- subsurface geologic probing (to make a 3D characterization of the subsurface structures),
- surface characterization (to measure surface roughness, reflectance to radar signals and to estimate topography),
- ionosphere sounding (to measure interaction between solar wind and the ionosphere).

To name some results of the MARSIS instrument, we can mention the following:

- revealing the layered subsurface structure of both polar caps (strongly suggesting there were oceans in distant history at these places) [23, pp. 98–102],
- estimating the volume of subsurface water ice in the polar cap [36],
- discovery of Medusae Fossae Formations (the youngest surface deposits) [23, pp. 102–105],
- mapping the ionosphere and verifying the ionospheric density models [23, pp. 105–110].

One surprising and unexpected utilization of the MARSIS instrument is given by the electron cyclotron echoes found in ionograms (see Section 1.3.5). It was found that the echoes often correspond to the strength of the magnetic field, effectively allowing to measure that field and compare it to its model. Another type of echoes, the oblique ionospheric echoes (see Section 1.3.3) were identified to correspond to the crustal magnetic field. Both these contributions were made by [24].

#### 1.1.4 Planetary Fourier Spectrometer (PFS)

PFS is IR-spectrometer (based on double-pendulum interferometer) operating in the range 1.2–42  $\mu\text{m}$  divided into two channels – the Short Wavelength (SW) channel (1.2–5  $\mu\text{m}$ ) and the Long Wavelength (LW) channel (5–42  $\mu\text{m}$ ). Its spatial resolution is 10 km for SW and 20 km for LW (from altitude 300 km). PFS uses

an onboard Fast Fourier Transform circuit to select only the data scientists are interested in [15, pp. 71, 86].

The objectives of this device are atmospheric studies like [15, pp. 115–116]:

- determining atmospheric composition (as it can detect e.g. H<sub>2</sub>O, CO and CO<sub>2</sub> spectra),
- solid-phase surface components detection,
- atmospheric dust measurements,
- capturing the vertical temperature–pressure profiles and dust and ice opacity.

The contributions made using PFS so far are for example [15, pp. 122–135]:

- measuring the atmospheric temperature (finding out that there is a rather complicated situation around the peak of Olympus Mons),
- measuring the surface temperature,
- counting the atmospheric dust content,
- observing temperature inversion effects,
- detecting methane in the atmosphere (which could imply either organic life or volcanic activity, which are both unexpected phenomena),
- proving that the south polar cap is made mainly from CO<sub>2</sub> ice,
- capturing the solar spectrum from the surroundings of Mars (which gives results irretrievable from Earth or near Earth).

### 1.1.5 SPectroscopy for the Investigation of the Characteristics of the Atmosphere of Mars (SPICAM)

The SPICAM instrument is made up of two spectrometers, one operating in the UV spectrum (118–320 nm) and the other in the near-IR spectrum (1.0–1.7 μm). Both these spectra provide information about (not only) H<sub>2</sub>O in the atmosphere [15, p. 95].

Many tasks have been assigned to SPICAM, the major of them being investigating ozone, H<sub>2</sub>O and aerosols vertical profiles in the atmosphere. These should help with e.g. [15, pp. 97–100]:

- constructing meteorological and dynamical atmospheric models,
- understanding the water vapour atmospheric cycles,

- characterizing processes of water escape from the atmosphere,
- investigating the interactions between surface and atmosphere,
- revealing the impact of aerosols on martian climate.

One of the latest surprises brought by SPICAM is that martian atmosphere is supersaturated with water vapour which further prepares conditions for water escape from the atmosphere [29]. Another unexpected result are nocturnal aurorae observed in the upper atmosphere, along with the (expected) NO recombination nightglow [7]. Other results involve:

- retrieving global spatial and temporal climatology of ozone [35],
- south polar cap observations [23, pp. 158–159],
- studies of UV dayglow [23, pp. 160–162],
- constructing the aerosol vertical profiles [23, pp. 175–180],
- observation of CO<sub>2</sub> clouds on the nightside [23, p. 178].

### **1.1.6 Analyser of Space Plasmas and EneRgetic Atoms (ASPERA–3)**

ASPERA–3 is an instrument designed to study the interaction between solar wind and martian atmosphere. It comprises of four separate detectors. The first detector is Neutral Particle Imager (NPI) measuring the energetic neutral atom (ENA) flux with high angular resolution. Another neutral atoms sensor, the Neutral Particle Detector (NPD), measures the neutral atom flux resolving energy and mass of the atoms. The other two instruments are aimed at electrically charged particles. The Electron Spectrometer (ELS) is a top-hat electrostatic analyzer, while the Ion Mass Analyzer (IMA) is an ion mass composition analyzer working with H<sup>+</sup>, He<sup>2+</sup>, He<sup>+</sup> and O<sup>+</sup> ions [15, p. 122].

ASPERA–3 should focus on [15, p. 122]:

- measuring ENAs in order to investigate the interaction between solar wind and martian atmosphere, to characterize the impact of plasma processes on atmospheric evolution and to obtain plasma and neutral gas distribution near Mars,
- measuring electrons and ions to complement ENA measurements to study the dynamics and structure of plasma and to provide solar wind parameters.

To present some results of ASPERA–3 we can mention the following:

- discovering that the solar wind penetrates much deeper in martian atmosphere than was believed, being one of the atmospheric ions escape mechanisms [4],
- detection of ENA jets caused by solar wind [23, pp. 208–209],
- observing the ENA flux during Mars eclipse which laid foundation of a new method to measure planetary exosphere [23, p. 209],
- proving there is a yet unidentified source of interplanetary ENAs [23, pp. 209–212].

### **1.1.7 Mars Express Orbiter Radio Science (MaRS)**

Opposite to the already described devices, the MaRS experiment does not have a dedicated physical device like a sensor or transmitter. Instead, it utilizes the antennas primarily used for communication to perform radio occultation experiments [15, p. 153]. It can use either MEX’s parabolic 1.6 m diameter High Gain Antenna or the smaller Low Gain Antennas attached to MEX. The receivers cannot be carried on board MEX, because they need to be on the opposite side of Mars than MEX is. Thus, the receivers are placed on Earth (Kourou, French Guayana; Darmstadt, Germany; Perth, Australia; three NASA’s Deep Space Network telescopes in Goldstone, USA; Madrid, Spain and Canberra, Australia). The experiment uses two frequency bands – the S-band at 2.1 GHz and the X-band at 7.1 GHz [15, pp. 153–154].

MaRS is intended to [15, p. 141]:

- sound the neutral atmosphere to derive vertical density, pressure and temperature profiles
- to sound the ionosphere (in order to get electron density profiles),
- to determine the dielectric properties of the surface,
- to detect gravity anomalies,
- to sound the solar corona at extra occasions.

MaRS contributed to e.g.:

- improving existing atmospheric global circulation models [23, p. 227],
- discovering the so-called “meteor layer” of atmosphere containing ionized metallic atoms brought into the atmosphere by meteoric impacts [23, p. 230],
- refining the knowledge of structure and density of martian crust [23, p. 234].

### 1.1.8 Beagle 2

Beagle 2 is the lander module MEX was equipped with [15, p. 165] (its visualization is shown in Figure 1.3). It detached from the spacecraft on December 19, 2003 (6 days before MEX orbit entry) and its touchdown was planned to December 25, 2003. However, it has not transmitted any signal after the martian atmosphere entry. As of February 2004 it was declared lost. No particular reason came out on inquiry into its fault [8].

To accomplish its main goal (searching for existing or former life, or at least for conditions allowing development of life in the past) it was equipped with the following scientific tools [15, pp. 165–187]:

- Gas Analysis Package: a mass spectrometer used for examining the surrounding atmospheric gases as well as rock and soil samples (heated in ovens in order to vaporize),
- X-Ray Spectrometer: used for studying the composition of rock and soil samples using X-Ray fluorescence spectrometry being able to detect metals like Fe, Mg, Al, Ti and others,
- Mössbauer Spectrometer: designed to analyze materials containing iron,
- Stereo Camera System: intended for acquiring stereoscopic images of the landing site in various spectral ranges,
- Microscopic Imager: should have provided one of the largest contributions to Beagle's main goal (by searching for microscopic fossils),
- Planetary Underground Tool: developed as a support for all the mentioned systems; it should have obtained soil samples using a 1.5 m long drill,
- there is also a grinder available for removing unwanted material from the samples or the surrounding surface.

There were also several sensors attached to Beagle 2 [15, pp. 188–191]:

- the oxidant sensor monitoring the oxidizing effects of martian atmosphere,
- the UV sensor capturing the UVA and UVB spectral ranges (which are lethal for organisms),
- the wind sensor recording the speed and direction of wind,
- the air pressure sensor with resolution 0.003 hPa,
- the air temperature sensor with accuracy about 0.01 K,
- the dust impact monitor measuring the magnitude and impact rate of dust particles.



Figure 1.3: Visualization of the Beagle 2 lander on martian surface. [5]

## 1.2 The MARSIS experiment

In this section, we discuss the individual parts of the MARSIS experiment. We briefly describe the physical background of the experiments as well as the technical solution of the measurement mechanisms.

### 1.2.1 Subsurface sounding

The subsurface sounding attempts to detect the borders of the cryosphere, which is the crust layer in which the temperature remains constantly under the water-freezing point. Such borders can be identified owing to different dielectric properties of liquid water, ice and atmospheric gases. The deeper border can be a water–ice interface. This is because the cryosphere ends at the depth where the internal planetary heat flow raises the temperature above the water-melting point. So if there is a liquid water reservoir under the cryosphere, it can be detected. This interface is expected to be at 0–5,000 m depth. On the other hand, the higher border can be formed by the desiccated megaregolith (martian soil) where the desiccation is caused by subsurface ice sublimation (estimated to be at depths between 0 and 1,000 m) [15, pp. 52–53].

As described in part 1.1.3, MARSIS can utilize a 40 m long dipole antenna as well as a 7 m monopole one. Only the dipole antenna is used for signal transmission (generating up to 10 W strong signal), and both antennas for signal

receipt. It can sound using one of the four subsurface frequency bands centered at 1.8, 3, 4 and 5 MHz, every one having 1 MHz bandwidth. When MEX operates on the dayside of Mars, the ionosphere does not allow to use lower frequency bands for sounding (see Section 1.2.3), so only the last two bands can be used. On the nightside, all four bands get through the ionosphere and allow to sound deeper subsurface. However, due to the limitations given by the MEX spacecraft, only echoes from depths up to 5–8 km can be detected [15, p. 57].

The subsurface sounder mode is based on the fact that the radar waves reflect not only on the surface, but also on subsurface dielectric discontinuities. In addition, the velocity of the waves decreases proportionally to the material loss tangent, the wavelength and the depth – which facilitates computing the depth of subsurface interfaces [15, p. 56].

### 1.2.2 Surface sounding

It arises from the previous paragraphs that the surface sounding mode is a “subset” of the subsurface sounding mode, taking only the “topmost” echoes into account. Therefore, no additional operation modes are present for just the surface sounding.

The surface sounding is used to create a topography of the surface with lateral resolution 5–9 km. This topography further serves for improving the accuracy of statistical topography models which describe the surface in the means of a random distribution of heights [15, p. 54].

### 1.2.3 Ionospheric sounding

The basic reason for studying the ionosphere is that it stops propagation of electromagnetic waves with frequencies below the local electron plasma frequency  $f_p$ . This frequency can be expressed as  $f_p = 8980\sqrt{N_e}$  Hz, where  $N_e$  is the local electron density in  $\text{cm}^{-3}$ . All vertical waves with frequencies below the maximum electron plasma frequency,  $f_p(\text{max})$ , are reflected back at a height with the same frequency as the waves have. This maximum is usually located at the heights 125–150 km and amounts up to 4 MHz on the dayside and 800 kHz on the nightside [15, pp. 55–56].

MARSIS uses two methods – a passive and an active one. The passive method measures thermal emission at the local electron plasma frequency. The active method – the one of our interest – sounds the ionosphere with the radar in 160 frequency steps ranging from 100 kHz to 5.4 MHz. With such sampling it is possible to construct vertical profiles of the electron plasma frequency (and also electron density). Besides the normal ionospheric sounding mode, MARSIS also provides a special interleaved mode switching periodically between the subsurface

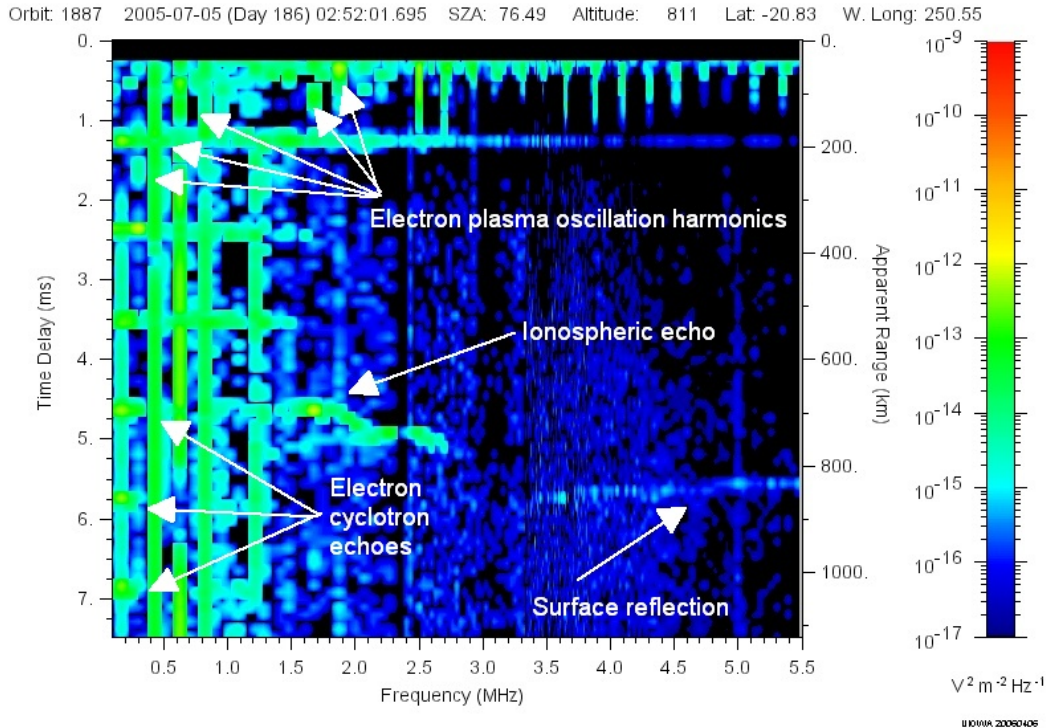


Figure 1.4: Example of a ionogram showing most of the detectable features like ionospheric echo, surface reflection, electron cyclotron echoes and electron plasma oscillation harmonics. No oblique ionospheric echo is present. The vertical axis shows delay time in ms, the horizontal axis stands for frequency in MHz and color codes the spectral density of the received electric field in  $\text{V}^2 \text{m}^{-2} \text{Hz}^{-1}$ . Based on real data obtained from [10].

sounding and ionosphere sounding modes. This yields a method to remove the ionospheric effects from the subsurface sounding results [15, p. 58].

Adding to the ionospheric and surface echoes, there are three more (unexpected [24, p. 1930], but useful) signal patterns detectable using the ionospheric sounding. Namely, oblique ionospheric echoes, electron plasma oscillation harmonics and electron cyclotron echoes. We will describe all of them in the following sections after presenting the concept of ionograms.

### 1.3 Ionograms

Ionograms are the basic visualization of the ionospheric sounding data. Akalin [1] defines ionograms in the following precise way:

Ionograms are produced by transmitting a short pulse at a fixed frequency,  $f$ , and measuring the received intensity at 80 consecutive values of the time delay,  $\Delta t$ , spaced  $91.4 \mu\text{s}$  apart. The frequency is then incremented and the process is repeated. For each of the

160 frequencies, quasi-logarithmically ( $\Delta f/f \approx 2\%$ ) spaced between 0.1 and 5.5 MHz, there are 80 delay time bins spaced 91.4  $\mu$ s apart. The bins start 162.5  $\mu$ s after the end of the sounding pulse. This gives 7.32 ms per one frequency and 1.26 s overall for the 160 frequencies (there is a small delay between the steps). Such complex sounding scan can be repeated every 7.54 s. Ionograms represent received intensity as a function of time delay and frequency. As shown by the ionogram in Figure 1.4, time delay is displayed in milliseconds along the vertical axis, frequency is displayed in megahertz along the horizontal axis, and the color bar represents the received electric field spectral density in  $V^2 m^{-2} Hz^{-1}$ .

Several more or less continuous patterns can be found in the example ionogram. Some of them form repetitious patterns. It can be also seen that the data are very noisy. The example ionogram is rather rare, because often just one or two such patterns occur in a single ionogram. There are also ionograms consisting entirely of noise. The subsequent sections will discuss all the patterns and their physical meaning.

### 1.3.1 Ionospheric echo

As seen in Figure 1.4, the ionospheric echo is a horizontally oriented non-straight line. It usually appears in the lower half of the ionogram (delay times about 4 to 5 ms). Under ideal conditions, its left end should start at the local electron plasma frequency, which is most often somewhere below 1 MHz. However, in practice the emitted power is too low at low frequencies and the echo vanishes in noise. Its right end should be placed at  $f_p(\max)$  frequency, where all higher-frequency waves pass to the surface [24, p. 1929].

There is often a sharp cusp at the right end of the echo. “The cusp occurs because the propagation speed of the wave packet (i.e. the group velocity) is very small over an increasingly long path length as the wave frequency approaches  $f_p(\max)$ ” [24, p. 1929]. On the other hand, the echo often does not extend up to  $f_p(\max)$  [24, p. 1930].

As we have mentioned earlier, it is possible to compute the local electron plasma frequency from the echo’s delay time, thus obtaining the electron density vertical profile. In order to extract the profile, it is needed to identify the curve fitting the echo. Automatic identification of such curve is one of the goals of this work. Especially correct estimation of the right end would be helpful if the cusp is present.

### 1.3.2 Surface echo

Similar to the ionospheric echo is the surface echo. It is placed lower than the ionospheric echo (because the ionosphere is closer to the sounder than surface is). Its left end is at the same frequency where the ionospheric echo's right end should be, i.e. at the  $f_p(\max)$  frequency. It should extend up to the right edge of the ionogram (since all frequencies higher than  $f_p(\max)$  penetrate the ionosphere) [24, p. 1929].

The same (but mirrored) cusp as in ionospheric echo should be present at the left end of the surface echo, caused by the same effect.

It is common that there is no surface echo in the ionogram. It can have several reasons. One of them is that the surface absorption of the radar waves increases with decreasing solar zenith angle (at angles lower than 40° the surface echoes are rare). Another way to stop the waves from returning to the sounder could be charged particles from solar flares ionizing the lower levels of ionosphere [24, p. 1930].

From surface echoes it is easy to read the apparent height over surface (omitting the cusp area). However, due to the frequent problems with absorption and low spatial resolution it is not practically useful for topography. At least, the surface-caused attenuation of the signal can be derived from the echo as well as the cusp may be identified, so we try to detect these echoes, too.

### 1.3.3 Oblique ionospheric echo

The first of unexpected features emergent in ionograms are oblique ionospheric echoes. An example of such echo is displayed in Figure 1.5. It is an echo of similar shape and horizontal boundaries as the ionospheric echo, but located a few ms lower in the ionogram. Often even lower than the surface echo – but the radar waves do not even reach the surface at the frequencies of the ionospheric echo.

An explanation of this effect is given in [24, pp. 1931–1933]. At locations with strong crustal magnetic field, this field forms bulges in the ionosphere. Such bulges, if lying aside the MEX track, reflect the waves from the sounder under such angle that the antenna records the reflections. However, since the track of these waves is not vertical, they may travel longer distances than to the surface before they return. An illustration of this effect is provided in Figure 1.6.

To detect oblique echoes in ionograms could be of some use, because they point to places with ionosphere bulges and strong crustal fields. However, deriving the shapes of the bulges or the crustal fields would be very complicated [24, p. 1932]. Therefore, we will not try to detect them in the task-specific algorithms devised in this thesis.

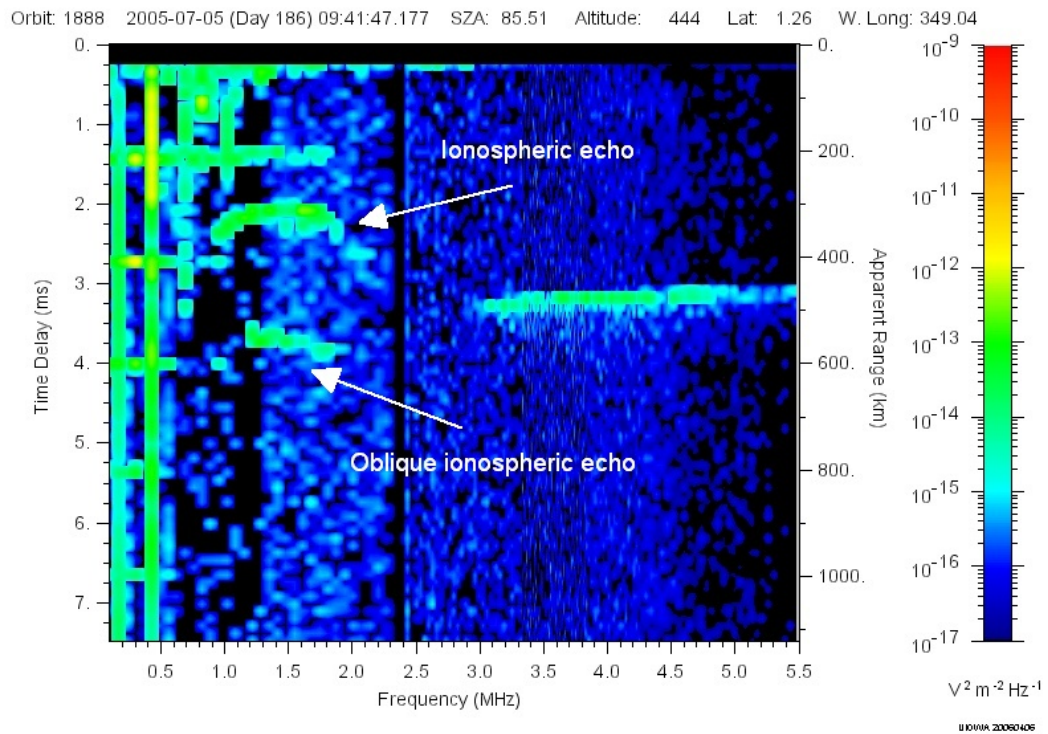


Figure 1.5: A ionogram containing oblique ionospheric echo. It is worth notice that the echo appears to origin under the surface level (because of the delay time higher than the delay time to surface). Based on real data obtained from [10].

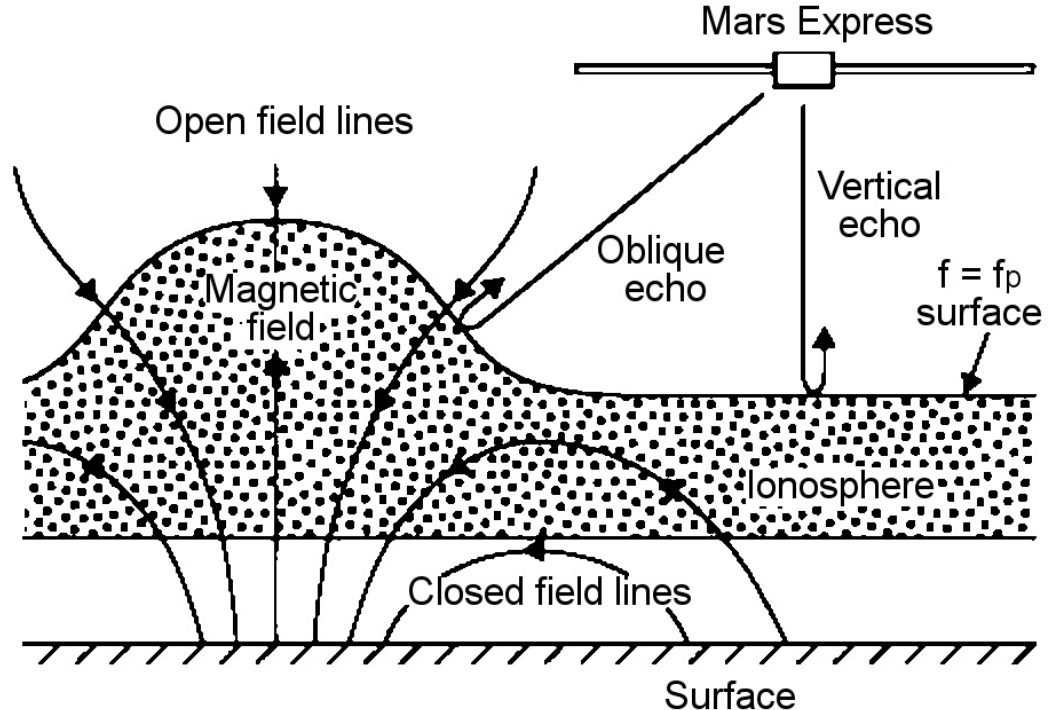


Figure 1.6: A ionospheric bulge created by strong crustal magnetic field can produce oblique ionospheric echoes. [24]

### 1.3.4 Electron plasma oscillation harmonics

Another surprise are repetitious straight vertical lines in ionograms, electron plasma oscillation harmonics (called also Langmuir waves [14, p. 2]). As can be seen in Figure 1.4, they appear near the top left corner of ionograms. They always start at the top of the image and continue towards the bottom; they may disappear on any time delay. Although they are mainly located in the left part of ionograms, occasionally they may repeat up to the right edge. More than 10 repetitions are, however, rare [14, p. 4].

It is stated in [24, p. 1929] that these echoes “are at harmonics of the local electron plasma frequency and are caused by the excitation of electron plasma oscillations, [...]. Even if the fundamental of the plasma frequency is not observed directly [...], the plasma frequency can still be determined from the spacing of the harmonics.” The reason why not only the base frequency is present, but also its harmonics, is described in [14, p. 2]: “Since the electron plasma oscillations are usually very intense, [...] the received waveforms are often severely clipped. The resulting distortion then introduces harmonics at multiples of the basic oscillation frequency.”

As all features detected by the ionospheric sounder, also plasma oscillation harmonics may not be present in a ionogram. There are three main reasons for it: when the local electron density is less than  $10 \text{ cm}^{-3}$ , when the plasma flow velocity is more than  $160 \text{ km/h}$  or when the temperature is greater than  $8,521 n_e \text{ K}$  ( $n_e$  stands for electron density in  $\text{cm}^{-3}$ ; this happens in solar wind) [14, p. 4].

Although the base oscillation frequency is occasionally captured in ionograms (when higher than  $100 \text{ kHz}$ , the sounder’s lowest frequency), it is apparently more precise to derive the frequency from the harmonics spacing (using multiple fit). That is what we will focus on in later chapters.

As a benefit, this method allows to measure the electron density down to  $10 \text{ cm}^{-3}$  which corresponds to heights up to  $1,300 \text{ km}$ . Such low densities could not be detected by the radar sounder.

### 1.3.5 Electron cyclotron echoes

The last unanticipated phenomenon appearing in ionograms are the electron cyclotron echoes. These are regularly-repeating straight horizontal lines in ionograms. They always start from the lowest sounding frequency (the left edge) and extend to frequencies up to  $2 \text{ MHz}$  [1, p. 3]. It can be observed in Figure 1.4 that the repetition can appear at the whole vertical range.

Comparing with the magnetic field model of Mars, Gurnett [24] determined that the repetition frequency of these echoes corresponds to local electron

cyclotron frequency  $f_c$ . That frequency can be expressed as  $f_c = 28 B$  Hz,  $B$  being the magnetic field strength in nT. Thus, knowing the repetition rate of the echoes, we are able to determine the strength of the magnetic field. That is a very important application, since MEX does not carry a magnetometer [24, p. 1930]. There is also a method to derive the vector component of the magnetic field under some conditions [1].

The origin of these echoes is described in [24, p. 1930]: “We believe that these echoes are caused by electrons accelerated by the strong electric fields near the antenna during each cycle of the transmitter waveform. The cyclotron motion of the electrons in the local magnetic field then causes these electrons to periodically return to the vicinity of the antenna, where they induce a signal on the antenna.”

Some constraints, of course, apply to the presence of cyclotron echoes in ionograms. Firstly, the magnetic field strength must be uniform on an area larger than the cyclotron radius (which is about 1 km). According to [24, p. 1930] this is easily satisfied. Further, the sounder’s minimum and maximum time delay resolution constrains the detectable field strengths. The minimum resolution of 182.2  $\mu$ s corresponds to field strength of 195 nT, while the maximum delay of 7.5 ms corresponds to field strength of about 5 nT. However, in practice the reasonable range for confident measurements is about 12 – 160 nT [1, p. 3].

Similarly to the plasma oscillation harmonics, we are interested in the period of repetition of these echoes. If we can compute it, we are able to compute the strength of the magnetic field and, in some cases, also its direction. We will also focus on detection of this period in our survey.

# 2 The detection problem

In the previous chapter, we have presented the physical background of ionograms. We have also shown the four major features that can be detected in them. In this part we try to make a transition to the technical point of view. Firstly we define the problem in the context of computer vision. Secondly we describe the data formats and finally we present the current situation about feature detection in ionograms and an analysis on how the problem could be solved.

## 2.1 Definitions

Now we are to seek for definitions of the basic terms used throughout the rest of this work. In order to precisely define the detection problem, we need to know the definitions of what a ionogram or its feature is. We also specify what attributes should a detection result have. Finally, we introduce some measures of quality of the detection along with formulating the problem.

### 2.1.1 Definition of ionogram

As stated in Section 1.3, a ionogram consists of electric field density measured at 160 frequencies and within 80 consequent time steps. Thus, we can treat a ionogram as a real-valued image (or a two-dimensional array) of dimension  $160 \times 80$ . The range of values at each pixel<sup>1</sup> is  $10^{-24}$  to  $10^{-10} \text{ V}^2 \text{ m}^{-2} \text{ Hz}^{-1}$ . However, it is obvious from the sample renderings in [10] that values lower than  $10^{-17}$  are considered to be background, so we can treat them as zeros. The horizontal indices are interpreted as the sounding frequency and they come from the range 0.1 – 5.5 MHz. The mapping from indices to frequencies is nonuniform and may differ for individual ionograms (it depends on the used frequency table; but a single table is preferred in most of the data). Every ionogram carries information about this mapping with it. On the other hand, the vertical indices map always to the same uniformly distributed values. They start at 162.5  $\mu\text{s}$  and go up to 7.32 ms using steps of height 91.4  $\mu\text{s}$  (assuming the lowest value to be at top).

As we are going to detect repetitious features, the ionogram with unevenly distributed frequency assignment would be impractical. To overcome this, we define our notion of “evenly sampled ionogram”. To get an evenly sampled ionogram from a normal ionogram, we linearize the frequency axis and then interpolate the “holes” in the image:

---

<sup>1</sup>We have not found an authoritative source for this information, but instead we deduced it from a large set of ionograms.

- We first extend each frequency column of the unevenly sampled ionogram by mapping the columns to a linear axis. The pixel width of the linear axis should be at least the frequency range (5.4 MHz) divided by the frequency width of the narrowest column (in order to allow every new column to have its width at least 1 px). We also stretch rows by the same amount to preserve aspect ratio. In practice we scale the ionograms so that the narrowest column has width 2 px to get a finer result. The size of such ionograms is then 1,012×506 px. See Figure 2.1 for illustration.
- Next we interpolate the new columns using linear interpolation. Suppose column  $i$  from the unevenly sampled ionogram stretched to columns  $j \dots j + k$  in the evenly sampled one. The values at column  $j$  are copied from  $i$  and for every column  $c \in < j + 1; j + k >$  its value is

$$v[c] = v[j] \cdot (1 - \frac{c - j}{k}) + v[j + k + 1] \cdot \frac{c - j}{k}$$

where  $v[c]$  denotes the vector of values at column  $c$ ,  $j$  and  $j + k + 1$  are the remapped columns corresponding to two originally neighboring pixels. In fact we just linearly interpolate the “holes” using the two nearest values from the original image. Figure 2.1 gives a visualization of this step.

- Then we perform the same interpolation vertically to fill missing values in columns. The final evenly sampled ionogram can be found in Figure 2.1.

This interpolation of course does not add any new information to the image, but it allows us to work on an image with both axes in uniform linear scale. We have chosen this kind of interpolation because it is the one used in the referential renderings available at [10]. We have simplified it by not caring about the values near edges, because they have insignificant impact on the results of detection. Nonetheless, any other kind of interpolation of missing pixels can be used as long as it preserves the values corresponding to the “original pixels” (e.g. plain pixel enlargement with copying the values instead of interpolating them).

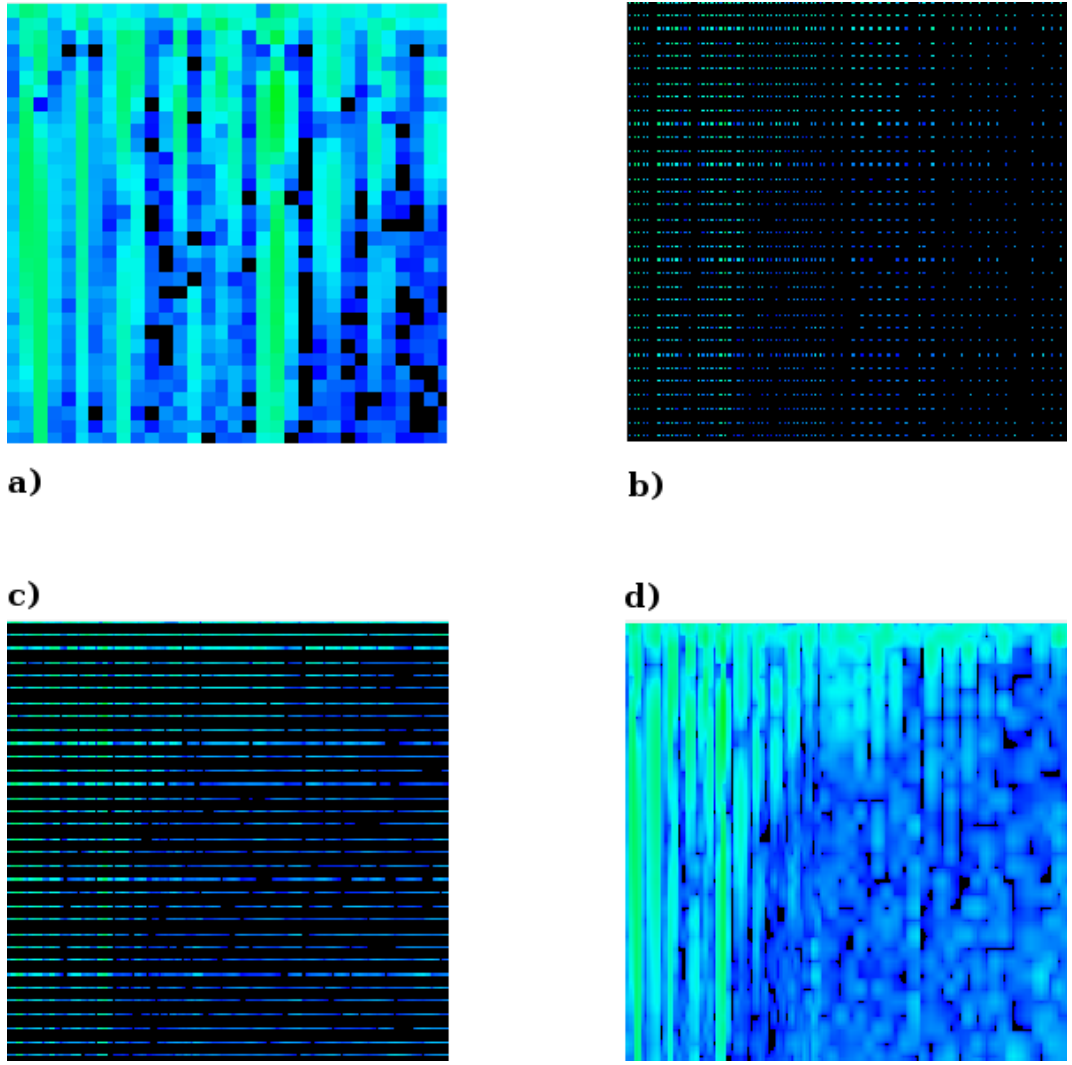


Figure 2.1: a) A part of the original unevenly sampled ionogram. b) The original ionogram mapped to a linear horizontal axis. Every original pixel is only mapped to one pixel in this image, the other pixels remain black. Here it is noticeable that values on the left are more dense than these on the right. This is due to the quasi-logarithmic distribution of sounding frequencies. c) Our evenly sampled ionogram after horizontal interpolation. d) Our evenly sampled ionogram after vertical interpolation. Data from orbit 3874, frame 0 [10].

### 2.1.2 Specification of the features to detect

We have listed four features of interest - ionospheric echoes (IE), ground echoes (GE), electron plasma oscillation harmonics (EPOH) and electron cyclotron harmonics (ECH) (in Section 1.3.3 we have already stated we omit oblique ionospheric echoes). We detect them based on the fact that they correspond to areas with significantly higher ionogram values than the background. However, ionograms are often very noisy, so it would be difficult (if not impossible) to define a single absolute threshold for telling whether a pixel belongs to a feature or not.

For verification purposes we obtained 115,495 manually tagged ionograms

from the Department of Surface and Plasma Science at Faculty of Mathematics and Physics, Charles University. These data come from 1,014 orbits during year 2007 (all orbits that year with some MARSIS data). In most of these ionograms the horizontal repeat period (corresponding to EPOH) is measured manually and the ionospheric echoes are marked. If no horizontal repetition period is present, that fact is recorded, too. Ionospheric echoes are marked in most cases. Unfortunately, we have no data for vertical periods or ground echoes (however, the latter seem to be detected very easily). Although being done manually and thus each feature being assessed subjectively, we deduced our rules for distinguishing interesting lines (which are either a feature or a part of a feature). Such line is several pixels wide (cca. 3–20 px) and at least that much pixels long (assuming the ionogram has dimension 1,012x506 px). Values on its skeleton (center line) are at least 10 times higher than those at its border. A line is also allowed to contain “gaps”, but no more than a third of the line’s length in sum. Moreover, every line should contain a value higher than cca.  $5 \times 10^{-15}$  (but not all points with higher values belong to a feature). Such definition looks, however, vague. So we propose additional specific constraints implying from the features we try to detect in our experiments.

An EPOH or ECH line must be almost straight and must go in exactly vertical or horizontal direction. In addition, one of its ends has to be near the top or left edge of the ionogram (no more than 5 px). ECH lines usually do not extend to frequencies above 2.5 MHz. A GE line follows approximately horizontal direction and does not have to be straight (due to terrain unevenness and the cusp; but mostly it is). It is placed in the delay time (or apparent height) corresponding to the height of the spacecraft over surface (that can be computed) which greatly helps in its detection. Finally, an IE line has also to be almost horizontal, but it may be substantially curved. It has to appear over the GE (if present).

Our statistical tests we conducted<sup>2</sup> on the data from year 2007 show that 99.5 % ionograms with some features have their mean value greater than  $2.452,16 \times 10^{-16}$ . Ionograms devoid of features have, of course, their mean values even lower than this value (in 21.5 % of cases). So we decided this value to be a threshold for telling a ionogram does not contain any features and we will not process it further. We did not choose lower reliability level because we do not want to throw away ionograms with some data present.

We also computed other statistical properties of ionograms that could help us better distinguish the features. We expected the maximum values in ionograms to be a reliable distinguishing mark, and standard deviations, too. As shown in Figure 2.2, neither maxima nor standard deviations show significant differences

---

<sup>2</sup>The application used for these tests is present on the attached CD in folder `programs/statistics` along with the data. See Appendix 1 for information on how to run it.

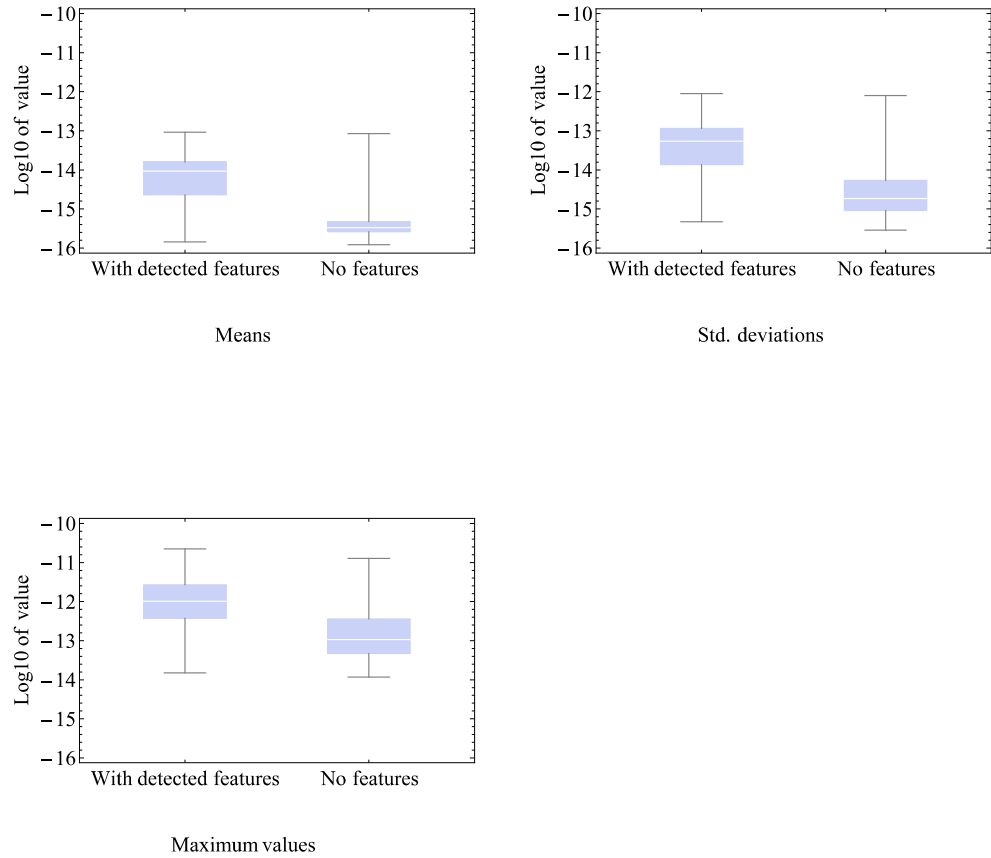


Figure 2.2: The distribution of means (top left), standard deviations (top right) and maximum values (bottom left) of individual ionograms from year 2007. The box plots show values for ionograms with features and without features separately. Data from [10].

between the data sets with features and without them. So they are not usable for distinguishing between the two data sets. We also made distributions of rather high values (over  $10^{-12}$ ) in relation to whether they are a part of a feature or not. The results showed almost identical distributions, but that can be due to the difficulty of reverse task. E.g. if we save just the period of an EPOH, it is not easily said if a data point belongs to this feature (we try to fit it on whole multiplies of the period, but we do not know the widths of the particular lines).

### 2.1.3 Specification of the detection results

Having an idea about how to recognize a feature, we can finally define the form of the results of our detection. Here it is important to declare we are not interested in the graphical shapes, rather we want to get results directly applicable in the physical models described in Section 1.3.

From Section 1.3.4 follows that to get the local electron plasma frequency from EPOH, it is sufficient to have the period of the harmonics. It is not important

how long or wide the harmonic echoes are, only the period of repetition. We denote this period as “hPeriod” (horizontal period) and measure it<sup>3</sup> in MHz.

Similarly, as noted in Section 1.3.5, to get the local electron cyclotron frequency from ECH, it is also sufficient to know the repetition period. We term this period as “vPeriod” (vertical period) and measure it in milliseconds.

The situation for ionospheric and ground echoes is quite the same. What we need is the time delay when the sounding wave first returned back with high intensity to derive height over ionosphere border or ground. We are also interested in the rightmost point of IE and leftmost point of GE (the cusp described in Section 1.3.1) to be able to read off the maximal electron plasma frequency  $f_p(\max)$ . The left end of the IE should start at the local electron plasma frequency, but it is read more reliably from EPOH. In conclusion, for both IE and GE we need to save the positions of all points on the top border of these echoes. We save it in ionogram coordinates, which are sounding frequency in MHz and delay time in milliseconds.

#### 2.1.4 Definition of the detection problem

Now we have all definitions needed to state the “detection problem”. Given a ionogram  $\mathcal{I}$ , find a (possibly empty) set of detection results  $\mathcal{R}$  corresponding to all features occurring in  $\mathcal{I}$ . Simultaneously minimize the number of false positives (found features not existing in fact) and false negatives (undetected existing features) and also minimize distance of the detection result values to the values of real features. As it is a multivariate optimization problem, we do not convert it to univariate optimization by specifying weights, we assess all three aspects separately.

Unfortunately, we do not have an oraculum divining the values of real features. Instead we have to replace it with the manually acquired data, which is the best approximation of the oraculum we can get. The drawbacks are, however, that the manually created data are not perfect, so the tested algorithms can seem to be better than in fact and vice versa simply due to the inaccuracy of the validation set. Until there are alternative ways to measure the observed values, manual verification is the best we have.

So we can reformulate the problem as finding detection results with minimum error on the verification set and with good generalization on other ionograms.

We can also generalize our whole problem (calling it the “generalized detection problem”) from ionograms to general images. Given an image  $\mathcal{I}$  and a set of rules  $\mathcal{S}$  describing the features to be found in  $\mathcal{I}$ , return the (possibly empty) set of detection results  $\mathcal{R}$  containing all features described by  $\mathcal{S}$  present in  $\mathcal{I}$ . To

---

<sup>3</sup>It may seem a little confusing to show a period in MHz, but it should rather be looked at as the difference of two sounding frequencies producing echoes.

measure the quality, a verification set of pairs  $(\mathcal{I}, \mathcal{R})$  should be provided. As a simplification we assume that  $\mathcal{S}$  contains only features that can be described using curves or curve structures (like repeating lines).

Roughly approximating, we can say the problem is a vectorization problem with known parametric expressions for some of the features in the image. As we show further, many vectorization techniques can be used for solving our problem.

## 2.2 Data formats

In this short section we describe our used input and output data formats and also the source for obtaining ionograms. This is the last step to do before we get to the analysis of our problem.

### 2.2.1 Data source

All data captured by the MARSIS instrument (and the others too) are stored in the Planetary Science Archive (PSA) run by ESA. It is located at WWW: <http://www.rssd.esa.int/index.php?project=PSA>. We access it using anonymous FTP access and the Active Ionospheric Sounding (AIS) data are stored at [ftp://psa.esac.esa.int/pub/mirror/MARS-EXPRESS/MARSIS/MEX-M-MARSIS-3-RDR-AIS-EXT1-V1.0/DATA/ACTIVE\\_IONOSPHERIC\\_SOUNDER/](ftp://psa.esac.esa.int/pub/mirror/MARS-EXPRESS/MARSIS/MEX-M-MARSIS-3-RDR-AIS-EXT1-V1.0/DATA/ACTIVE_IONOSPHERIC_SOUNDER/). There are subfolders for every 10 orbits in the archive (named e.g. RDR193X for orbits 1930–1939). In these subfolders there are files named `FRM_AIS_RDR_(orbit number).LBL` which contain metadata about the orbit. Each such metadata file references a data file named `FRM_AIS_RDR_(orbit number).DAT` containing the sounding data.

We remark that for some orbits there are no AIS data available when MARSIS was not instructed to operate. E.g. from the cca. 1,300 orbits in year 2007 we processed manually there are 1,014 orbit data files.

### 2.2.2 Input files format

The metadata (.LBL) files are text files formatted according to the Planetary Data System (PDS) v3 format defined in [27]. Although the format can be quite complex, to parse the metadata we are interested in, just a simple line-by-line text parser is sufficient.

The orbit data (.DAT) are stored according to the binary format specified in Attachment 3.1. Every orbit data file contains frames which can be interpreted as individual ionograms. There are 30 – 400 frames per orbit depending on the observation conditions and other possibly interfering MEX operations.

Every frame further consists of 160 columns records each of 80 elements. Every column record (corresponding to one sounding pulse) carries information about the exact time the sounding started, the sounding frequency and much more parameters we are not interested in.

We implemented a reader for the .LBL and .DAT files that returns the corresponding Java objects. It is located on the attached CD in folder `programs/AIS-Data-Reader`, namely classes `Ionogram` and `AISLBLProductReader`. See Appendix 1 for information on how to run it.

### 2.2.3 Output files format

To be consistent with the input files, we have decided to use 1 result file per orbit, too. We name it `TRACE_(orbit number).XML` and place it to the same folder as the source .DAT file. However, contrary to the input data files, we have decided to store the results in text files using XML (XML Markup Language) structure. There are two main reasons. The first is the most important one – the result files are small in comparison to the data files, so we can afford some inefficiency introduced by text encoding. The second reason is straightforward – XML files are easy to read even for humans and parsing them is a simple task.

The structure of the file is shown in Attachment 3.2 using the XML Schema language. The main element represents the whole orbit, and there are elements for every frame from the input file. These elements contain the values we detect, namely in elements `<hPeriod>`, `<vPeriod>`, `<ionospheretrace>` and `<groundtrace>`. If no EPOH or ECH is present, the corresponding values are set to 0.0 to indicate absence of these features. This is also the structure of the manually measured data we got.

We provide a set of Java classes able to convert between the output XML and Java objects. These classes can be found on the attached CD in folder `programs/AIS-Result`. The classes make use of the widely used Java And XML Bindings v2 (JAXB2) de/serialization framework [26]. See Appendix 1 for information on how to run it.

## 2.3 Automated detection

This section mentions the current status of solving the problem. Then we follow with an analysis of the problem and explore the ways possibly leading to an automated detection solution. These open ideas and propositions conclude this chapter.

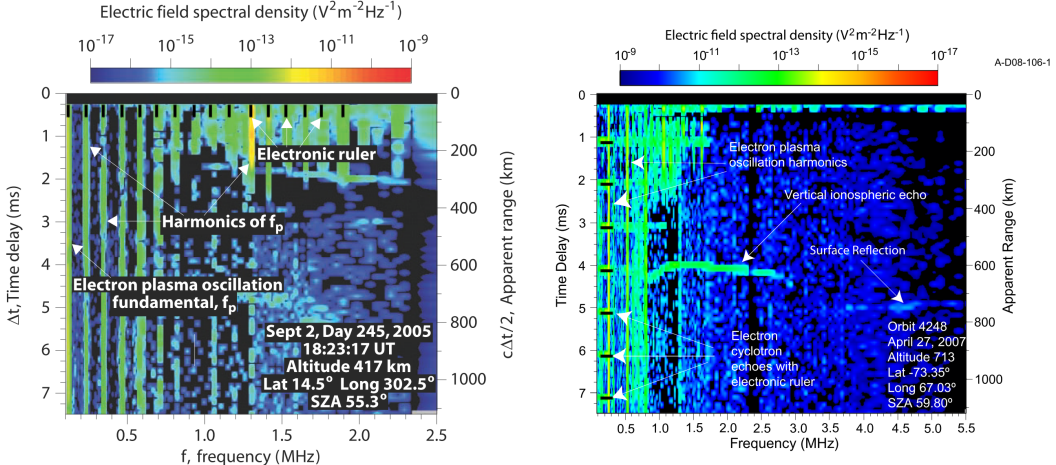


Figure 2.3: Previews from the software for manual measurements of horizontal and vertical spacings. In the left image there are horizontally placed black tick marks near the top border for measuring EPOH [14]. The right image shows vertically repeating black tick marks near the left edge which serve for measuring ECH period [1].

### 2.3.1 Current ways of solving the problem

As far as we know there is currently no fully automated software solving the formulated problem. All the measurements are performed manually by visual tools. We think it is due to the requirement on high precision of the detected values. The Department of Physics and Astronomy, University of Iowa, developed a software called “MARSIS Ionogram Survey” for manual recording of visual measurements. However, using the software requires authorization from the department.

Nevertheless, some screenshots illustrating the basic idea were published [14, 1]. We provide them in Figure 2.3. As can be seen in both images, there are evenly spaced black tick marks laid over a ionogram. The period between these tick marks is easily adjusted by moving the computer’s mouse. The operator then displays a ionogram and matches the tick marks against the repetition period he recognizes in the ionogram. This way the vertical and horizontal period can be easily measured – only a 1% error in the detected frequency can be reached [14, p. 2].

Digitization of the IEs and GEs is done by selecting the top edge using mouse and a tool that draws piecewise-straight horizontal lines. The result then may look like stairs with unevenly long steps, which is what the top edge of ionograms most often looks like. These lines are then sampled using the original sampling of the ionogram and saved one point per sounding frequency.

The absence of an automated tool for this work was the main reason for choosing this topic of our thesis. Computer vision provides plenty methods for similar tasks. We discuss them in the next section.

### 2.3.2 Proposed solutions

To start exploring the fields of computer vision that offer useful algorithms for our problem, we first need to narrow down the classification of this problem. It is clear that we do not have to look outside the computer vision field, because that is what our task is about – automatically doing something that is relatively easy for human sight.

At first glance our task of automated detection may resemble pattern recognition (PR). There is, however, a problem with not having the patterns to match. What we have is a parametric expression for the features. And the general pattern recognition methods work only with a limited, final and constant set of patterns. Fortunately, looking at the problem closer yields a way to use these methods at least for the repeating lines. If we take a PR method invariant to pattern scale, we can use repeating lines with unit period as the pattern and let the algorithm match it. If the algorithm allows getting the scale of the pattern, the real repetition period is easily found. Due to the relatively small resolution of the non-uniform ionograms (which are sufficient for finding IEs and GEs) we would be also able to generate a list of shapes an IE or GE can have. Using this list as the set of patterns could bring us some results (but there are imminent cases of false positive detections).

The second field we consider helpful to solve similar tasks is vectorization. Converting bitmaps to vectors is exactly what our problem needs. A lot of work in this field is, however, done in vectorization of technical drawings which is based on assumptions not applicable to our problem. For example the technical drawings have relatively low level of noise (which ionograms do not have) and they have thin, accurate lines (most often drawn by hand with a ruler). The lines in ionograms are most fuzzy and noisy. Thus, edge detection commonly used in these algorithms does not give useful results applied to ionograms. But these algorithms are not worthless. If we manage to perform a thinning or skeletonization algorithm (described further) on ionograms, suddenly the fuzzy lines could become thin and accurate and thus suitable for use with these algorithms. Noise reduction could also help.

Using a specific property of EPOHs and ECHs we could reach good results using a very simple technique. If we compute the row or column sums of the ionogram values (the electric field density), we get a profile with high peaks corresponding exactly to the repeating lines. The other two features (IEs and GEs) do not affect these profiles much (because they are relatively smaller compared to EPOHs and ECHs; only IEs in ECHs may cause problems), as well as noise does not. Having the peaks detected it is needed to estimate the period (since the peaks may be slightly displaced). We propose several methods for such detection: computing a periodogram of the peaks distribution (see Section 3.3.1

for definition), fitting a sine wave to the peaks or taking an average period. It is also desirable to use the “height” of the peaks as weights for the mentioned methods (since the higher the peak is, the higher is the probability it really belongs to the desired line and not to noise or other features). With the knowledge of the height above surface, row sums can also be used to decide if GE is present and to find its left end. This is because ECHs usually do not extend to the right half of ionogram where GEs usually appear, so we can take only the right half of the image. It is possible to proceed without the height information, too, but the task simplifies if we use it. The last feature, IEs, could also be detected using row and column sums, but it would need cancellation of all three preceding features from the image, which does not seem feasible. Without the ECH lines cancelled out the echo would not be reliably distinguishable from the harmonics line – in fact, it can even merge with them in the row sums.

We also consider evolutionary algorithms (EAs) as a method worth trying. In EAs, we initialize a population of individuals (representing the detection results) randomly. Then we let them recombine and mutate using some defined operators. We periodically select the best of them (according to a defined fitness function) to survive to the “next round”, let them reproduce and start the whole process over. The algorithm ends when the individuals converge to an acceptable solution. It is apparent what an individual should look like – a vector with values for hPeriod, vPeriod and some more points defining the IE and GE. If we manage to design good recombination and mutation operators, as well as fitness, the results could be interesting.

We have just presented the areas of interest, in which we perform our research. For every area we propose several algorithms, describe them and test on the current data from year 2007. The subsequent chapters are dedicated each to one area.

# 3 Lateral histograms

This chapter treats of lateral histograms, which in our case simplify to row and column sums of the image. Although being very simple in principle, the lateral histograms show as a strong and robust method for EPOH and ECH detection. The largest part of its success, however, depends on the methods for estimating the period from the histograms. We present several such methods, perform experiments on them and compare them based on the experimental results.

## 3.1 Lateral histograms applied to ionograms

Lateral histograms are a little more general notion than we need in ionograms. We first provide the general definition and then we look for the more specialized one. We also observe a great simplification brought to this method by the nature of ionograms.

### 3.1.1 Definition

The general definition of lateral histograms is that “the lateral histogram technique involves projecting an image on two or more axes by summing pixel intensities [...] and using the resulting histograms to identify objects in the image.” [12] As can be seen, the title “histograms” does not have exactly the common meaning (counts of points with similar values). The slightly changed definition uses sums instead of counts and the “similar values” mean the same position with respect to the chosen axis.

To detect EPOHs and ECHs it is sufficient to take into account only the vertical and horizontal axes (whereas the definition allows for arbitrary axes). This is because EPOHs are strictly vertical lines and ECHs strictly horizontal. Summing up rows or columns, it can be clearly seen that in most cases the harmonic echoes generate high peaks in these histograms. The height of the peak corresponds to the length of the harmonic echo line as can be seen in Figure 3.1.

### 3.1.2 Simplification in the case of ionograms

The general definition assumes we are looking for point-like structures (given by 2 coordinates) and thus requires computing the histogram along at least two axes. From two histograms both 2D coordinates can be determined, but often there are ambiguities in the solution (for features overlapping in the direction perpendicular to an axis) [12, chap. 13]. The removal of such ambiguities is not trivial.

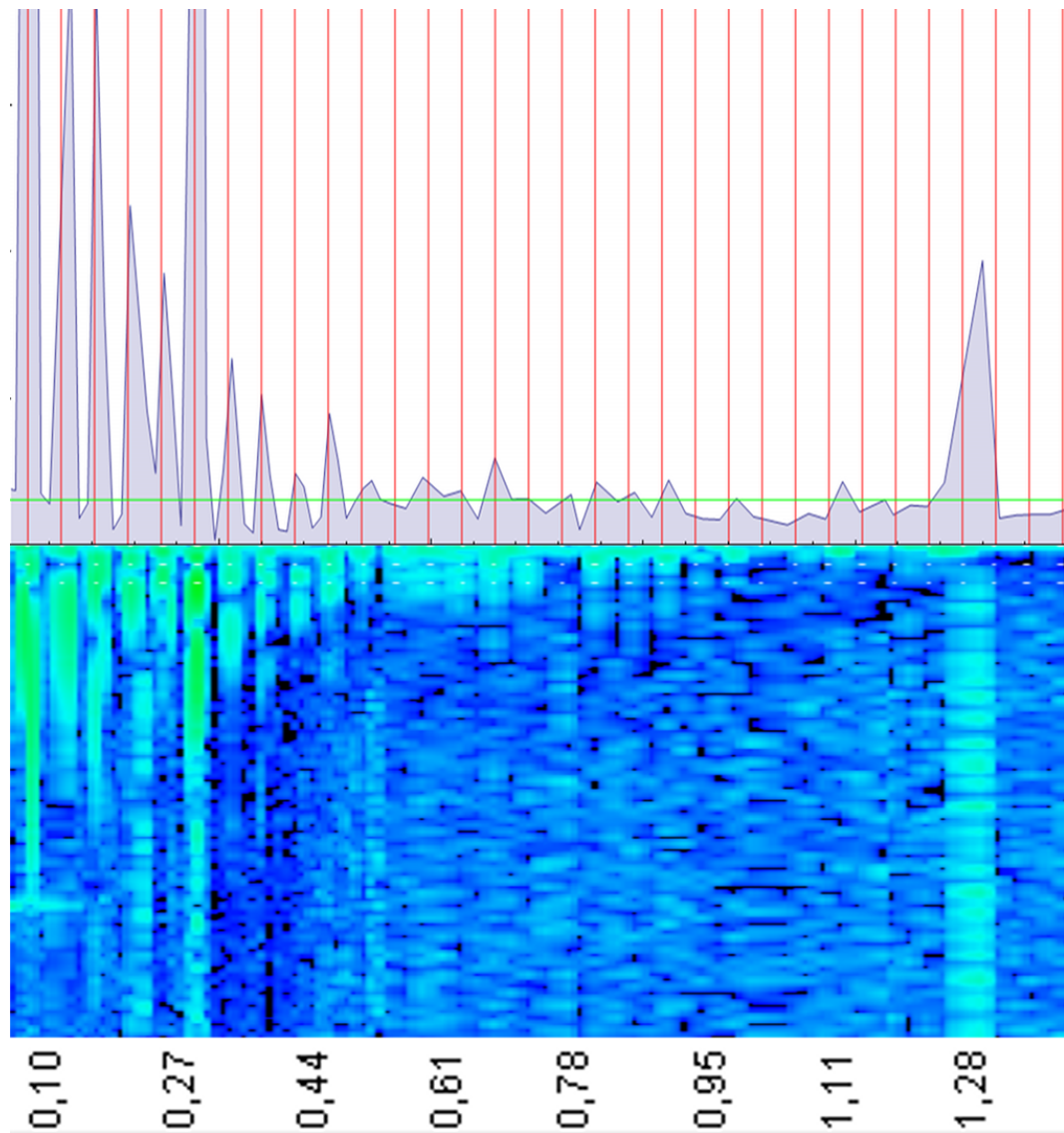


Figure 3.1: The column sums of a part of ionogram. The ionogram below is displayed along the sounding frequency scale in MHz. The top part shows the column sums at the frequencies from ionogram. The red lines represent the harmonics of the manually measured repetition period. They very closely correspond to the peaks in column sums. The green horizontal line denotes the mean value of the sums.

Fortunately, in the ionogram case, only one axis is sufficient for every feature, since we are not interested in the length of the echo lines. Having the one histogram, detection of its peaks is all that is needed. Not all peaks in the histogram correspond to a harmonics line, some lower of them can be caused by noise. We call the peaks from harmonic lines “real peaks” and the others “false peaks”. Our methods try to minimize the influence of false peaks by weighing them.

## 3.2 Implementation

We implemented our feature detector using the lateral histograms technique on evenly sampled ionograms. It can be found on the attached CD in directory `programs/detector-summing`. See Appendix 1 for information on how to run it.

### 3.2.1 Finding and filtering the peaks

Due to the properties of both EPOH and ECH we can reduce the problem to working on the left half of ionograms. It may happen that some EPOHs stretch beyond the half, but in such cases there have to be lots of other harmonic lines in the left part (since the harmonics are the stronger the closer they are to the base frequency). As all ECHs start at the left border and usually are not very long, cutting the image in half is also possible.

As stated above, not all peaks in the histogram belong to the harmonic echoes. In order to find only the high peaks, we first filter out 50 % of the row/column sums with the lowest values. We should be able to detect periods of length 2 bins (the original unevenly sampled frequency columns), which would give just the 50 % threshold. As can be derived from [1, p. 3], detecting periods less than 2.5 bins is impractical in the time domain, which yields threshold of 60 %. As echoes in the frequency domain have to be sparser (due to the quasi-logarithmic spacing and quantization to bins), we can use this threshold, too.

With the uninteresting values filtered out (by setting them to zero) we can proceed to finding the peaks. The algorithm is rather simple, it just treats as a peak every data point with both neighboring values lower or equal to it. Once it finds a peak it zeroes out both non-increasing sequences neighboring to it (to get rid of non-strict maxima). What remains are the highest local maxima of the histogram. A visualization of the steps is shown in Figure 3.2.

### 3.2.2 Using the peaks of row/column sums

In an ideal case the set of peaks would contain all the harmonic lines positions and no more. In practice, noise and data inaccuracies introduce some false peaks. As

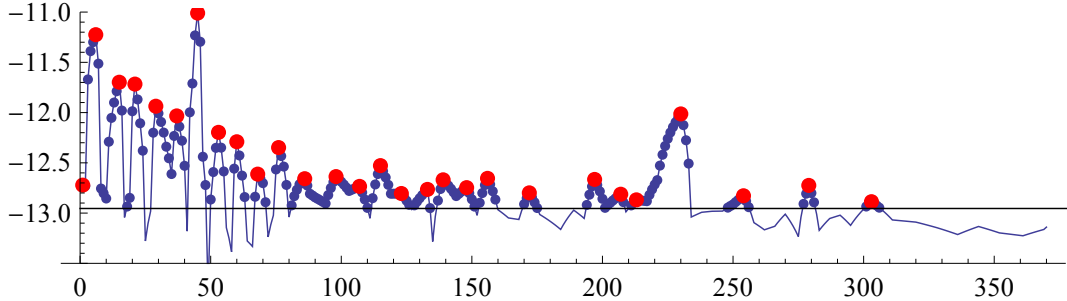


Figure 3.2: The steps to do when filtering the peaks within column sums in order to find the highest peaks. The blue lines are the original column sums. The blue dots are the column sums over the 0.6-quantile represented by the black line. We seek for the peaks among these values. The peaks are marked with the larger red dots.

a heuristic to tell if a peak comes from harmonic lines, we can look at its height. The echo lines are often long and have their values more than 10 times higher than the background around them. Both these facts contribute to greater values of the row/column sums. For EPOH, if there are some ECH lines or an IE in the image, they disappear in the peaks list. It is because they are perpendicular to the EPOH lines and so may fill up the space between EPOHs, but in the frequency domain, their contribution is relatively small in comparison with the contribution of the EPOH lines. Ground echoes are almost completely discarded by cutting the ionogram in half. Similarly, while detecting ECH lines, the EPOH lines should cause no trouble. However, an IE can cause problems because it usually adds a very high and broad peak to row sums. This is a caveat of using this method to detect ECHs. The only way to overcome this seems to be to narrow down the examined portion of ionogram to a range about 0.1–0.8 MHz (where the IE usually does not occur). The drawback is the narrowing allows for more important effects of noise. So we rather examine the whole half of the ionogram with bearing in mind that if other algorithms discover an IE in the ionogram, the vPeriod is most malformed.

We should also be able to recognize when there are no data of interest in the ionogram. Using just row/column sums it would have been, however, more a statistical than algorithmic decision. We could say what levels of row/column sums mean no feature is present. Or we could try to measure the “ruggedness” of the histogram to tell if there are some peaks. But we chose to rather not do such estimates and instead allow false positive detections. Removal of the false positives can be done later by comparing to the results of other methods more suitable to tell that a feature is not present at all.

So we have the peaks and their heights as heuristics (telling us the probability of them to come from a line of interest). Combining these, we are finally able to estimate the repeat frequency. The last remaining task is to find a method taking peak positions and their weights (corresponding to their heights; we always

normalize the weights) and computing the most probable period. The following section lists our three implemented methods – the periodogram method, sine wave least squares fitting method and period averaging.

### 3.3 Period estimation

A period estimation method has to count with the fact that there are some peaks missing and some of them are extra. It should hold that the extra peaks have relatively low weights. On the other hand, some “regular” peaks can also have low weights. Again, there is no absolute rule on the weights of the peaks.

#### 3.3.1 Periodograms

The first proposed method is determination of the period from periodograms. Periodograms are defined in [37] for time series data. We slightly modify this definition to fit our purposes. Treat our set of peaks as a random variable  $X$  measured at pixels  $t_i$  along the axis (pixels without a peak yield zeros, the other ones). The measured values are denoted  $\{X_i = X(t_i) : i = 1, 2, \dots, N_0\}$ . In our case,  $N_0$  is the number of pixels along the axis.

Having all the peaks the same unit height, we can now try to search for a sine wave with unit amplitude that would cross all the peaks. As the heights of the peaks are equal to the amplitude, it is required that the wave crosses the peaks exactly at its local maxima. Since sine is a periodic function and reaches its maximum once a period, the period of repetition should be equal to the period to be found between peaks.

We first present a simple form of periodogram which is fundamental for understanding the principles behind periodograms. The periodogram of random variable  $X$  at frequency  $\omega$  is by [37] defined as:

$$P_X(\omega) = \frac{1}{N_0} \left| \sum_{j=1}^{N_0} X(t_j) \exp(-i\omega t_j) \right|^2 \quad (3.1)$$

$$= \frac{1}{N_0} \left[ \left( \sum_{j=1}^{N_0} X(t_j) \cos \omega t_j \right)^2 + \left( \sum_{j=1}^{N_0} X(t_j) \sin \omega t_j \right)^2 \right] \quad (3.2)$$

The explanation of the meaning of this expression is “that if  $X$  contains a sinusoidal component of frequency  $\omega_0$ , then at and near  $\omega = \omega_0$  the factors  $X(t)$  and  $\exp(-i\omega t)$  are in phase and make a large contribution to the sums in equation (3.2). At other values of  $\omega$  the terms in the sum are randomly positive and negative, and the resulting cancellation yields a small sum.” [37, p. 836] This means that there should be high distinctive peaks of  $P_X$  near the  $\omega$  values close

to the frequency of the sinusoid.

Another important fact is that it is sufficient to evaluate  $P_X$  at a finite set of frequencies to get the correct one. This set is, according to [37, p. 850], as follows:

$$\{\omega_n = 2\pi n/N_0 \mid n = -N_0/2, \dots, +N_0/2\}$$

The meaning of this set can be understood in this way: “The fundamental frequency,  $\omega_1 = 2\pi/N_0$ , corresponds to a sine wave with frequency equal to the whole interval  $N_0$ . This is roughly the lowest frequency about which there is information in the data. The so-called Nyquist frequency,  $\omega_N = \frac{1}{2}(2\pi/\Delta t) = \pi$  ( $\Delta t = 1$  is the sampling of the interval) is roughly the highest frequency about which there is information, because  $\Delta t$  is the shortest time interval spanned.” [37, pp. 850–851].

Finally, we present a modified version of periodogram devised in [37]. The new definition has several benefits, but for us it is important that it is phase invariant (since we do not know the phase of the signal). The definition by [37, p. 838] is the following:

$$P_X(\omega) = \frac{1}{2} \left\{ \frac{\left[ \sum_{j=1}^{N_0} X(t_j) \cos \omega(t_j - \tau) \right]^2}{\sum_{j=1}^{N_0} \cos^2 \omega(t_j - \tau)} + \frac{\left[ \sum_{j=1}^{N_0} X(t_j) \sin \omega(t_j - \tau) \right]^2}{\sum_{j=1}^{N_0} \sin^2 \omega(t_j - \tau)} \right\}, \quad (3.3)$$

where  $\tau$  can be computed from

$$\tan(2\omega\tau) = \left( \sum_{j=0}^{N_0} \sin 2\omega t_j \right) \Bigg/ \left( \sum_{j=0}^{N_0} \cos 2\omega t_j \right) \quad (3.4)$$

Summed up,  $\tau$  is the term providing phase invariance. The form (3.3) has also better statistical properties and can be used with uneven sampling (which we do not need)[37, p. 849].

Our implementation passes the list of peaks to the periodogram function  $P_X$  and computes the periodogram for the  $N_0$  frequencies  $\omega_n$ . Then it selects the highest peak and computes the period belonging to it. An example of the periodogram is shown in Figure 3.3. Unfortunately, we have not found out how to incorporate peak weights to the algorithm. We tried multiplying every peak with its weight. Compared to the unweighted case, the results were even worse. We also tried to select the best peak among the 10 highest peaks (according to the mean of the column sums corresponding to the peaks). But the assessment method is probably not so strong, so in most cases the total result remains unchanged.

Our implementation can be found on the attached CD in folder

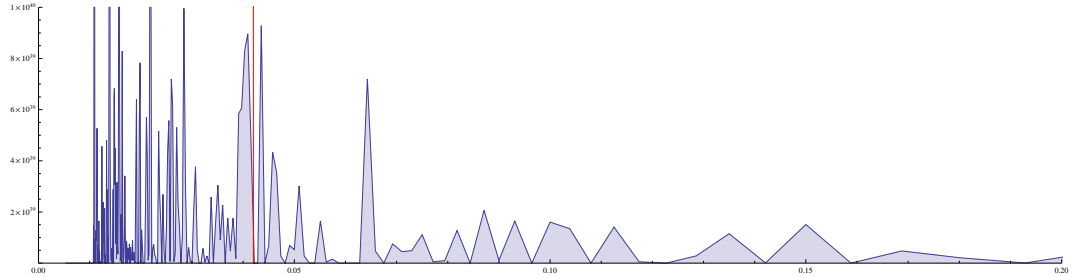


Figure 3.3: The periodogram computed from the first ionogram in orbit 3874. The horizontal axis does not, however, show the frequency  $\omega$  as is usual for periodograms, but it is already converted to correspond to the repetition period. The red vertical line is at the place of the manually measured repetition frequency. It can be seen it tends to be near a large peak, but unfortunately at lower frequencies there are higher peaks that lead to incorrect results. The peaks in the left part are cropped at the top in order in interest of clarity.

[programs/detector-summing](#). See Appendix 1 for information on how to run it. The results of the detection can be found also on the CD in subfolders of folder `data/` – they are files named `TRACE_(orbit number)_SUM_PERIODGRAM.XML`.

To assess the quality of the periodogram period estimation method, we perform two tests. In the first one we just measure the absolute difference between the estimated value and the manually acquired one; we denote it  $E_A$ . For simpler interpretation of the results we show the absolute error in ratio to the manually acquired value to get a percentage (for estimated period  $p_e$  and manual period  $p_m$  we compute  $E_A = |p_e - p_m|/p_m$ ). This is a nonuniform scaling, but it makes sense to require lower absolute errors for shorter periods.

We noticed that the estimated periods are often notable shorter than the target ones. After investigating the cause of this problem (which would render this method practically worthless) we found an explanation. Probably due to the (unweighted) false peaks the method tries to fit a sine wave which would go through all the real peaks as well as the false ones. This behavior makes the estimated periods be a “1/integer” fraction of the real period (eg.  $1/2$ ,  $1/3$ ,  $1/4$ ,  $\dots$ ). This result looks interesting, because at least it allows us to considerably reduce the search space. Due to this property we also compute the second statistic  $E_P$  (we call it the period corrected error) – the error of the nearest integer multiple of the estimated period (that is  $E_P = |round(p_m/p_e) \cdot p_e - p_m|/p_m$ ).

The results of these tests are shown in Figure 3.4. As can be clearly seen, the absolute error  $E_A$  with median 68 % shows the results to be completely useless. On the other hand, the period corrected error with median 4.5 % and 0.75-quartile 7.6 % looks like a relatively good result. Average computation time (covering also the GE detection detailed in Section 3.5) is about 0.65 s per ionogram of size  $1,012 \times 506$  px.

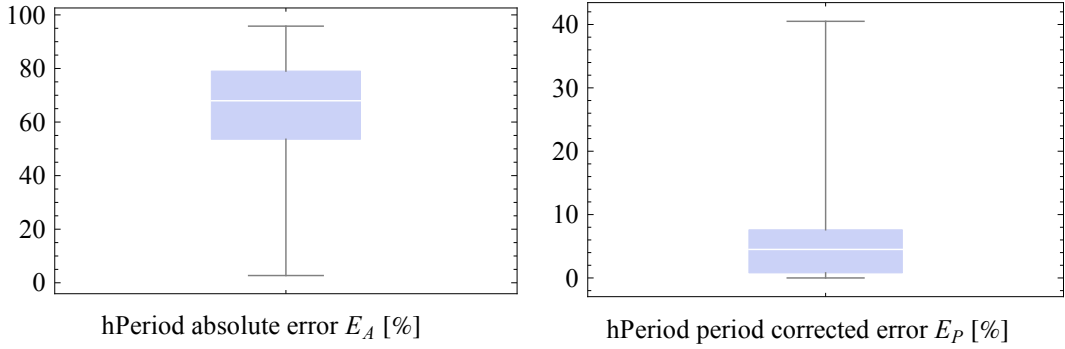


Figure 3.4: The errors of period estimation using the periodogram method. The tests were conducted on a set of ionograms from orbits 3836–4000. The left chart displays the absolute error  $E_A$  with the 0.25-quartile = 53 %, median = 68 % and the 0.75-quartile = 79 %. The right chart shows the period corrected error  $E_P$  with the 0.25-quartile = 0.8 %, median = 4.5 % and 0.75-quartile = 7.6 %.

To sum it up, the periodogram-based period estimation is not perfect for our task. On the other hand, its results can be utilized by other methods to scale down the search space. One more drawback is it only searches a fixed set of periods to try out.

### 3.3.2 Sine wave least squares fitting

The idea of fitting a sine wave to the peaks leads us to another algorithm. While the classical least squares fitting methods are suitable only for linear models to fit, there are also ways to do a similar fitting with nonlinear functions. One of these algorithms is the Levenberg-Marquardt algorithm introduced in [31].

We start with defining the model to fit, which is

$$E(y) = f(x; \beta_1, \dots, \beta_k) = f(x, \boldsymbol{\beta}) \quad (3.5)$$

where  $E(y)$  is the expected value. We simplify our case to a single variable, whereas [31, p. 431] describes the problem for any number of variables. Denote the peak values we have as  $(Y_i, X_i)$ ,  $i = 1, \dots, N_0$ . Then the least squares minimization problem is to find an assignment of  $\beta$  that minimizes the error function

$$\Phi = \sum_{i=1}^n [Y_i - \hat{Y}_i]^2 = \|\mathbf{Y} - \hat{\mathbf{Y}}\|^2, \quad (3.6)$$

where  $\hat{Y}_i$  are the estimated values given by  $E(y)$  [31, p. 431].

For the algorithm we need the Jacobian matrix

$$J_j = \frac{\partial f(x)}{\partial b_j}, \quad j = 1, \dots, k, \quad (3.7)$$

where  $b_j$  are the current estimates of  $\beta_j$ . We also need the vector

$$\mathbf{g} = \left( (Y - f(x)) \frac{\partial f(x)}{\partial b_j} \right) = J^T(\mathbf{Y} - f(\mathbf{b})), \quad j = 1, \dots, k. \quad (3.8)$$

Both these notions are defined in [31, p. 433].

With these definitions we can describe the iterative Levenberg-Marquardt algorithm. We select the damping factor  $0 < \lambda^{(1)} \leq 1$  (some guides on its selection are provided in [31, p. 437]). The initial parameter vector  $\mathbf{b}^{(1)}$  has to be guessed and passed to the algorithm. In every iteration  $r$  we solve the set of linear equations

$$(J^{(r)T} J^{(r)} + \lambda^{(r)} I) \boldsymbol{\delta}^{(r)} = \mathbf{g}^{(r)} \quad (3.9)$$

for the difference  $\boldsymbol{\delta}^{(r)}$  which is used in the next iteration to construct  $\mathbf{b}^{(r+1)} = \mathbf{b}^{(r)} + \boldsymbol{\delta}^{(r)}$ . Using  $\mathbf{b}^{(r+1)}$  we can update  $\Phi^{(r+1)}$ . Then we choose new damping factor  $\lambda^{(r+1)}$  and proceed to the next iteration (as described in [31, pp. 437–428]). The iterations are repeated until either a maximum number of iterations is exceeded, if  $\Phi$  converges to 0 or if we encounter a local minimum of  $\Phi$ .

With a good initial guess, the algorithm converges to the global minimum of  $\Phi$ . However, the algorithm may often lodge in a local minimum of  $\Phi$  instead. But by good strategy for choosing  $\lambda$  it should be robust enough [31, pp. 437–428].

In our experiments we used the implementation of the Levenberg-Marquardt (LM) algorithm provided by the library Apache Commons Math 3 [2]. In addition to the above described algorithm, it also supports weighing the data (by simply incorporating the weights in the error function), which is exactly what we want. It also contains a procedure for getting the initial guess on parameters based on computation of several definite integrals and using linear least squares method. This method is described in the source code [3].

In our approach we try to fit a sine wave with unit amplitude against the peaks with unit height. In order to magnify the effect of the weights, we also make square roots of all of them and then normalize them. This way more mid-value weights can affect the fitting, which usually helps, as we have observed.

Since we have both minimum and maximum constraints on the frequency, we have to tell these constraints to the LM algorithm. As the Apache Commons implementation does not support imposing constraints to the optimized variables, we simulate such constraints by returning  $\pm 1$  derivative in direction  $\omega$  for values

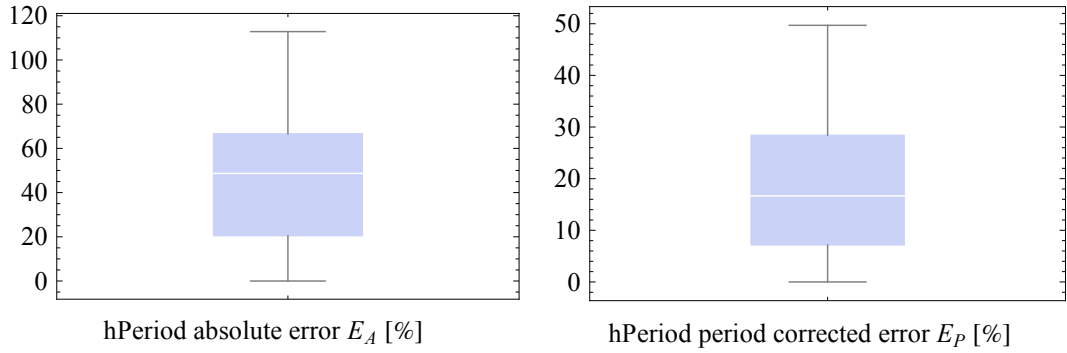


Figure 3.5: The errors of period estimation using the sine wave fitting method. The tests were conducted on a set of ionograms from orbits 3836–4000. The left chart displays the absolute error  $E_A$  with the 0.25-quartile = 20.4 %, median = 48.7 % and the 0.75-quartile = 66.7 %. The right chart shows the period corrected error  $E_P$  with the 0.25-quartile = 7.1 %, median = 16.7 % and 0.75-quartile = 28.4 %.

outside our boundaries. This seems to be sufficient.

Our implementation can be found on the attached CD in folder `programs/detector-summing`. See Appendix 1 for information on how to run it. The results of the detection can be found also on the CD in subfolders of folder `data/` – they are files named `TRACE_(orbit number)_SUM_FITTING.XML`.

For quality assessment we use the same two metrics as for periodograms – the absolute error  $E_A$  and the period corrected error  $E_P$ , since the fitting algorithm also suffers from returning “1/integer” multiples of the real period. The reason is the same as for periodograms – with some false peaks, a lower error can be achieved by doubling (or tripling, ...) the frequency.

Final results of our tests are shown in Figure 3.5. Similarly to the periodograms, the absolute error  $E_A$  with median 49 % renders the results to be worthless. In contrast to the periodograms, however, the period corrected error with median 17 % and 0.75-quartile 28 % also cannot be treated as a good result. From these results it seems the curve fitting method is not a good solution to our problem. We think it may be due to the false peaks (although they should have small weights). Average computation time (covering also the GE detection detailed in Section 3.5) is about 3 s per ionogram of size  $1,012 \times 506$  px. It is really slow compared to the other methods, mainly due to the iterative base of this method.

### 3.3.3 Period averaging

The last proposed way to determine the period from peaks and their weights is a method we call “period averaging”. It utilizes a completely different approach than the previous methods.

On the input we again have the peaks with their weights. We first calculate the “neighbor distances” – distances of the peaks being just one next to the other. This is the base for our approach. Each such distance gets a weight assigned that is equal to the weight of its right peak. In the ideal case without false peaks and with peaks for every harmonic line, simply computing a weighted average of these distances should give us the correct period. As we do not work with ideal data, we devised a method how to overcome the difficulties with false peaks and missing peaks for harmonic lines.

When we would just do a weighted average of the distances, a few missing harmonic lines could completely mislead the result (as well as the false peaks). E.g. we can take a period of 2 units. Then having 4 harmonics spaced correctly at the 2 units distance would give the correct period of 2 units. If these 4 lines were followed by 2 more lines spaced at 4 units (as if they were 4 lines and 2 of them disappeared, which is common in ionograms), then the average period would be  $(4 \cdot 2 + 2 \cdot 4) / 6 = 8 / 3 \doteq 2.67$ , which is an error of 33.3 %. This is unacceptable. Even the weighing does not help in this case because regular harmonic lines should have large weights (opposite to the false peaks which should have low weights and should not influence the result much).

We investigated the ionograms and we deduced that almost never more than a third of the harmonic lines is missing in the left half of ionograms (which we use in the rows/columns summing algorithm). So if we rule out (rounded off) 35 % of the longest distances, we should not remove many correctly spaced peaks. On the other hand, all the long distances caused by missing harmonics should be eliminated. If there are no harmonics missing, we just eliminate some distances corresponding to the correctly spaced peaks, but since no harmonics are missing there must be several other correct distances left with high weights. As said earlier, false peaks should be smoothed out by their low weights.

So, with the resting 65 % of distances, we re-normalize their weights. And with these weights we just evaluate the weighted arithmetic average of the distances and the harmonics period is found.

Our implementation can be found on the attached CD in folder `programs/detector-summing`. See Appendix 1 for information on how to run it. The results of the detection can be found also on the CD in subfolders of folder `data/` – they are files named `TRACE_(orbit number)_SUM_QUANTILE.XML`.

For quality evaluation we again use the absolute error  $E_A$  and the period corrected error  $E_P$ . We expect the difference between  $E_A$  and  $E_P$  to be

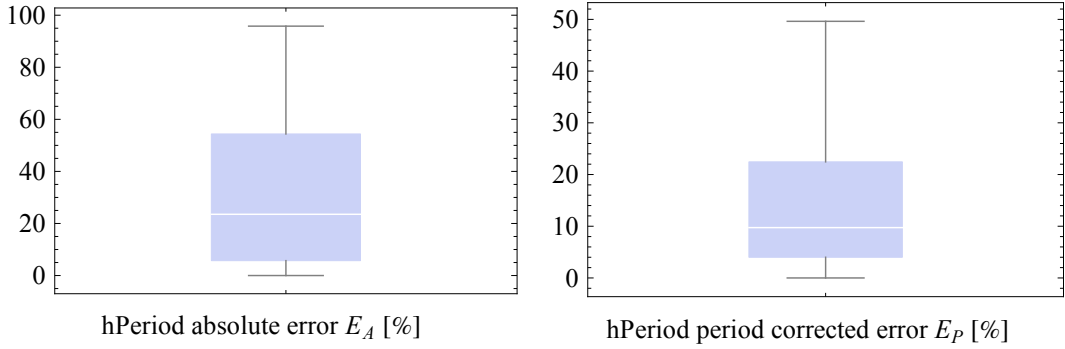


Figure 3.6: The errors of period estimation using the period averaging method. The tests were conducted on a set of ionograms from orbits 3836–4000. The left chart displays the absolute error  $E_A$  with the 0.25-quartile = 5.7%, median = 23.5% and the 0.75-quartile = 54 %. The right chart shows the period corrected error  $E_P$  with the 0.25-quartile = 4 %, median = 9.9 % and 0.75-quartile = 22.4 %.

significantly lower than in the previous two methods (especially  $E_A$  should be lower). That is since the period averaging should not tend the yield fractions of the real periods.

The outcomes of our tests are shown in Figure 3.6. As expected, the absolute error  $E_A$  is lower, with median 23.5 % being the best of the methods tested so far. What is a small disappointment for us is a relatively high  $E_P$  – with median 9.73 % and 0.75-quartile 22.5 % it is not the best one. Average computation time (covering also the GE detection detailed in Section 3.5) is about 0.56 s per ionogram of size  $1,012 \times 506$  px.

### 3.3.4 Combining the methods

Taking into account the properties of the periodogram-based and average-based methods, there emerges a new, rather powerful and robust method for period estimation. As the periodogram-based method is good at determining the “period corrected” period (denote it  $p_p$ ), the average-based method well estimates the “magnitude” of the period (denoted  $p_a$ ). By magnitude we mean that the estimated period is not a fraction of the manually measured period  $p_m$  (it is near this value, but still with a rather large error as mentioned in the previous section).

So we have the period  $p_p$  about which we know that there exists an integer coefficient  $c$  such that  $c \cdot p_p \doteq p_m$ . And we also know  $p_a \doteq p_m$  but with a larger error. So we propose to compute the integer  $c$  as  $\hat{c} = \text{round}(p_a/p_p)$  and then determine

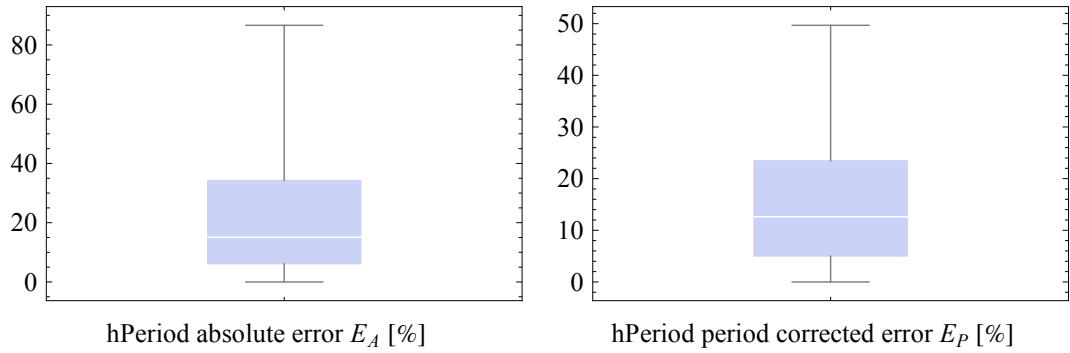


Figure 3.7: The errors of period estimation using the combined periodogram- and averaging-based method. The tests run on a set of ionograms from orbits 3836–4000. The left chart displays the absolute error  $E_A$  with the 0.25-quartile = 6.1 %, median = 14.3 % and the 0.75-quartile = 34.6 %. The right chart shows the period corrected error  $E_P$  with the 0.25-quartile = 5.2 %, median = 11.7 % and 0.75-quartile = 22.9 %.

the period as  $\hat{c} \cdot p_p$ .

Because the periodogram-based method uses only a constant set of periods to try, we would be limited by these values, which could lead to unnecessary errors in the result. For this reason we weight both periods into the final result  $\hat{p} = 0.5 \cdot p_a + 0.5 \cdot \hat{c} \cdot p_p$ .

Our implementation can be found on the attached CD in folder `programs/detector-summing`. See Appendix 1 for information on how to run it. The results of the detection can be found also on the CD in subfolders of folder `data/` – they are files named `TRACE_(orbit number)_SUM_COMBINED.XML`.

The evaluation again consisted of expressing the absolute error  $E_A$  and the period corrected error  $E_P$ . Our expectation is that the difference between  $E_A$  and  $E_P$  is insignificant, because there should remain almost no estimates needing the “period correction”. Also  $E_A$  should be the lowest observed so long.

The results of our tests are presented in Figure 3.7. Following our expectations, the absolute error  $E_A$  is low; with median 14 % it is the winner of this chapter. On the other side, 0.75-quartile 35 % is not as good as we expected. The small difference between  $E_A$  and  $E_P$  is validated – the median of  $E_P$  is 11.7 % (which means that there still remained some results influenced by period correction, which is interesting). Average computation time (covering also the GE detection detailed in Section 3.5) is about 0.60 s per ionogram of size 1,012×506 px.

### 3.4 Vertical periods detection

All the results presented above refer to the horizontal periods (EPOHs). Since we have no reference data for the vertical periods, we could not conduct such large statistical tests. So we just checked the estimated results with a small set of vertical periods extracted manually by ourselves. The result is not very good. The vertical periods used to be rather large (even a third of height of the ionogram and more), so there are not many echoes and the noise effects become significant.

Also, the often stronger (and mainly longer) EPOHs behave as strong noise in this case – they can even cause filtering out some vertical lines. As the EPOH-caused noise near the top part of the image (where EPOHs are the strongest) may reach rather high values, the real vertical peaks near bottom may fall under the 60 % level used for peaks selection.

To conclude, we can say the detected vertical periods do not have significant relation to the real periods and their detection fails. As long as we do not have some larger set of verification data, solving this problem looks, however, impractical.

### 3.5 Ground echo detection

This last part of chapter about lateral histograms usage is dedicated to ground echo detection. With the knowledge of the current spacecraft height above surface (computed from the ephemeris data), we can predict the vertical position of ground echoes.

The first thing we do is decide whether a GE is present. This has two steps. The first is rather simple and only takes determining if the height above surface is less than the maximum detectable height. This boundary is limited by the 7.32 ms height of the vertical axis of ionograms. As radio waves spread approximately with the speed of light near Mars, the height corresponding to time delay  $\Delta t$  is  $c \cdot \Delta t / 2$  (the  $/2$  for the signal path to surface and back,  $c$  stands for the speed of light in vacuum). Supplying the maximum time delay to this equation, the maximum height at which a GE may appear is 1,098 km.

The second decision step is based on row sums. We work only with the right half of the ionogram since this is where a GE may occur. We further divide the half of ionogram into two parts – the rows near the possible GE occurrence (up to 20 px under than the possible occurrence for a ionogram sized  $1,012 \times 506$  px), and other rows. Computing mean values of the electric field density in these two groups gives us a very good guiding principle for telling if a GE is present or not. If the mean in the group near GE is more than 2 times higher than in the rest, we tell a GE is present. The threshold value 2 was determined experimentally

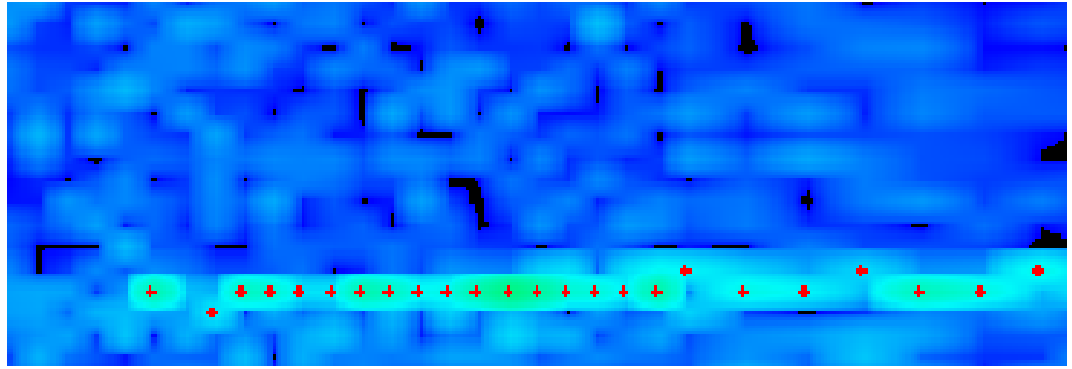


Figure 3.8: An example of detected ground echo (the red dots). A cut of frame nr. 46 from orbit 3874.

and seems to give good performance.

When we know we should look for a GE, we start at the right side of the ionogram and progress to its left (but we stop in the half). We begin on the row corresponding to the predicted GE occurrence. At every column we look at the values in the current row and 10 px under it and pick the highest of them. If this value is higher than the mean of rows near the possible GE as computed earlier, we consider it a part of the GE. If so, we also change the “actual row” to the row with the highest value before proceeding to the next column – this makes the algorithm a tracking algorithm able to track even the cusp that may occur.

The results of the algorithm as described slightly differ from what we have defined as a result of GE detection. We defined the result should be the top edge of the GE and this algorithm instead finds the part with the highest values, which is commonly the centerline of the echo. We do not consider this a big problem because it may be processed further using a simple postprocessing, which, however, needs deeper information on the properties of the edge. As for the shape of the detected echo, it is nearly the same as the shape of the top edge of the GE.

As stated in Section 2.1.2, we have not been provided with GE referential data. So the only assessment method available is visual comparison of a small set of detection results. As far as we can say, we have not found any ground echo with even a little bad shape, all the inspected ones precisely copied the shape of the ground echo. An example of a detected ground echo is given in Figure 3.8. We have also found no false negative detections (false positives may occur, though it is not frequent).

## 3.6 Summary of lateral histogram methods

We have presented a single method using the lateral histogram approach. This method may utilize one of the four proposed period estimation methods, of which the best is the combined method. As its error of estimation is about 14% we

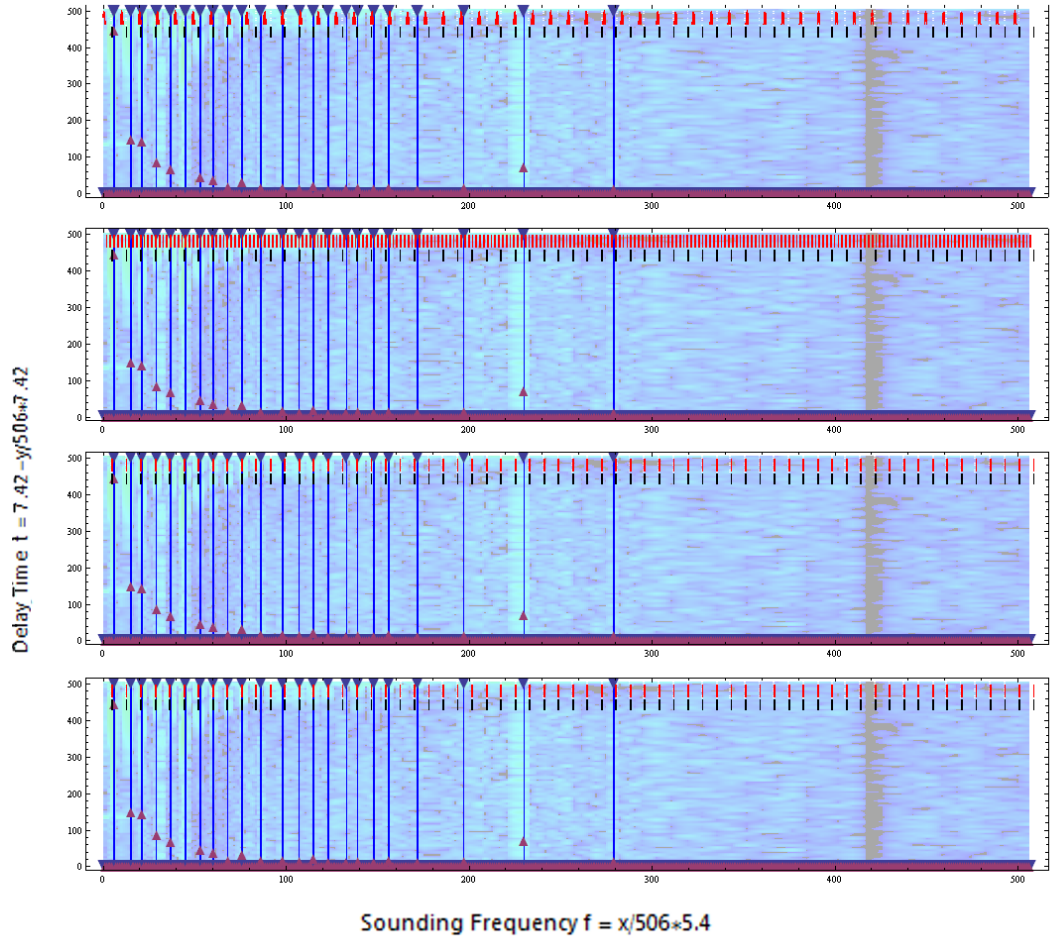


Figure 3.9: A comparison of periods detected by the presented methods. Red ticks are the detected period. Black ticks denote the manually acquired period. Blue triangles as well as the blue lines correspond to peaks detected in the column sums. Purple triangles (with the tip up) are at positions corresponding to peak weights (multiplied by two for better visibility). From the top: the periodogram method, sine wave fitting method, average period method and the combined method. The ionogram in background is frame 0 in orbit 3874. Axis labels are in pixels of the evenly sampled ionogram.

cannot say it is a perfect method (since manual tagging reaches a 1% error level), but it is definitely not worthless. All methods but sine wave fitting can be said to be relatively fast, with computation times about 0.6 s per ionogram. An example comparison of the detected periods is given in Figure 3.9.

We have also stated the the detection of the vertical period is a serious problem for this method. It needs further investigation to discover some really helpful noise-reducing techniques.

At last we have presented a very good way of determining the ground echoes in ionograms. It seems reliable as well as precise. We consider this as a good enough method for the precise measurements, although its detection error could not be validated due to the lack of reference data.

# Conclusion

# **Appendix 1**

**Running the programs on the attached CD**

# Bibliography

- [1] AKALIN, F. et al. Dayside induced magnetic field in the ionosphere of Mars. *Icarus*. March 2010, 206, 1, pages 104–111. ISSN 00191035. doi: 10.1016/j.icarus.2009.03.021. Available from: <http://linkinghub.elsevier.com/retrieve/pii/S0019103509001316>.
- [2] APACHE. *Math - Commons Math: The Apache Commons Mathematics Library*. In *Apache Commons* [online], 2013. [Accessed 04/10/2013]. Available from: <http://commons.apache.org/proper/commons-math/>.
- [3] APACHE. *[Apache SVN] Contents of HarmonicFitter*. In *Apache Commons Math 3* [online], 2013. [Accessed 04/10/2013]. Available from: <http://svn.apache.org/viewvc/commons/proper/math/trunk/src/main/java/org/apache/commons/math3/fitting/HarmonicFitter.java?view=markup>.
- [4] BARABASH, S. et al. Martian atmospheric erosion rates. *Science (New York, N.Y.)*. January 2007, 315, 5811, pages 501–3. ISSN 1095-9203. doi: 10.1126/science.1134358. Available from: <http://www.ncbi.nlm.nih.gov/pubmed/17255508>.
- [5] BEAGLE\_2. *Beagle 2 lander*. In *Space In Images* [online], 2002. [Accessed 03/24/2013]. Available from: [http://spaceinimages.esa.int/Images/2001/11/Beagle\\_2\\_lander](http://spaceinimages.esa.int/Images/2001/11/Beagle_2_lander).
- [6] BERTAUX, J. L. et al. First detection of O<sub>2</sub> 1.27 μm nightglow emission at Mars with OMEGA/MEX and comparison with general circulation model predictions. *Journal of Geophysical Research*. March 2012, 117, pages E00J04. ISSN 0148-0227. doi: 10.1029/2011JE003890. Available from: <http://www.agu.org/pubs/crossref/2012/2011JE003890.shtml>.
- [7] BERTAUX, J.-L. et al. Nightglow in the upper atmosphere of Mars and implications for atmospheric transport. *Science (New York, N.Y.)*. January 2005, 307, 5709, pages 566–9. ISSN 1095-9203. doi: 10.1126/science.1106957. Available from: <http://www.ncbi.nlm.nih.gov/pubmed/15681381>.
- [8] BONACINA, F. *Lessons Learnt From Beagle 2 And Plans To Implement Recommendations From The Commision Of Inquiry*. In *Ireland / ESA in your country* [online], 2004. [Accessed 03/24/2013]. Available from: [http://www.esa.int/ESA\\_in\\_your\\_country/Ireland/Lessons\\_learnt\\_from\\_Beagle\\_2\\_and\\_plans\\_to\\_implement\\_recommendations\\_from\\_the\\_Commission\\_of\\_Inquiry](http://www.esa.int/ESA_in_your_country/Ireland/Lessons_learnt_from_Beagle_2_and_plans_to_implement_recommendations_from_the_Commission_of_Inquiry).

- [9] CHEVRIER, V., POULET, F., BIBRING, J.-P. Early geochemical environment of Mars as determined from thermodynamics of phyllosilicates. *Nature*. July 2007, 448, 7149, pages 60–3. ISSN 1476-4687. doi: 10.1038/nature05961. Available from: <http://www.ncbi.nlm.nih.gov/pubmed/17611538>.
- [10] CHICARRO, A. *MEX MARSIS AIS data*. In *Planetary Science Archive* [online], 2005. [Accessed 03/26/2013]. Available from: <ftp://psa.esac.esa.int/pub/mirror/MARS-EXPRESS/MARSIS>.
- [11] CLARK, S. *Mars Express back in business at the red planet*. In *Spaceflight Now* [online], 2012. [Accessed 03/20/2013]. Available from: <http://www.spaceflightnow.com/news/n1202/15marsexpress/>.
- [12] DAVIES, E. *Machine vision: theory, algorithms, practicalities*. Academic Press, 2004. Available from: <http://books.google.com/books?hl=en&lr=&id=uY-Z3v0RugwC&oi=fnd&pg=PP2&dq=Machine+Vision+Theory,+Algorithms,+Practicalities&ots=QKr9RaONB9&sig=RMTdAvtoT2pxrv0ckCYDlOMKoaI>.
- [13] DOUTÉ, S. et al. South Pole of Mars: Nature and composition of the icy terrains from Mars Express OMEGA observations. *Planetary and Space Science*. January 2007, 55, 1-2, pages 113–133. ISSN 00320633. doi: 10.1016/j.pss.2006.05.035. Available from: <http://linkinghub.elsevier.com/retrieve/pii/S0032063306001243>.
- [14] DURU, F. et al. Electron densities in the upper ionosphere of Mars from the excitation of electron plasma oscillations. *Journal of Geophysical Research*. 2008, 113, A7, pages A07302. ISSN 0148-0227. doi: 10.1029/2008JA013073. Available from: <http://www.agu.org/pubs/crossref/2008/2008JA013073.shtml>.
- [15] ESA. *Mars Express: the scientific payload*. Noordwijk, Netherlands: ESA Publications Division, 2004. Available from: [www.esa.int/esapub/sp/sp1240/sp1240web.pdf](http://www.esa.int/esapub/sp/sp1240/sp1240web.pdf). ISBN 92-9092-556-6.
- [16] ESA. Mars Express Master Science Plan Part I - Introduction. Technical Report 1, 2004. Available from: <http://www.rssd.esa.int/SB/MARSEXPRESS/docs/MSPDOC/MSPOverviewDocumentation-PartI.pdf>.
- [17] ESA. *Mars Express Radar Deployment Postponed*. In *ESA Science & Technology* [online], 2004. [Accessed 03/20/2013]. Available from: <http://sci.esa.int/science-e/www/object/index.cfm?fobjectid=35021>.

- [18] ESA. *Mars Express 2nd Boom Deployed*. In *ESA Science & Technology* [online], 2005. [Accessed 03/20/2013]. Available from: <http://sci.esa.int/science-e/www/object/index.cfm?fobjectid=37608>.
- [19] ESA. *Mars Express and the mystery of Phobos*. In *ESA Kids Liftoff* [online], 2010. [Accessed 20. 3. 2013]. Available from: [http://www.esa.int/esaKIDSen/SEM8534KV5G\\_Liftoff\\_1.html](http://www.esa.int/esaKIDSen/SEM8534KV5G_Liftoff_1.html).
- [20] ESA. *Mars Express steadily returns to routine operation*. In *ESA Our Activities* [online], 2011. [Accessed 03/20/2013]. Available from: [http://www.esa.int/Our\\_Activities/Operations/Mars\\_Express\\_steadily\\_returns\\_to\\_routine\\_operation](http://www.esa.int/Our_Activities/Operations/Mars_Express_steadily_returns_to_routine_operation).
- [21] ESA. Programmes in Progress. *Bulletin Space for Europe issue 148*. 2011, pages 72–73. Available from: <http://esamultimedia.esa.int/multimedia/publications/ESA-Bulletin-148/pageflip.html>.
- [22] ESA. *Fact Sheet*. In *ESA Science & Technology* [online], 2013. [Accessed 03/20/2013]. Available from: <http://sci.esa.int/science-e/www/object/index.cfm?fobjectid=47364>.
- [23] FLETCHER, K., WITASSE, O. *MARS EXPRESS: The Scientific Investigations*. Noordwijk, Netherlands: ESA Communication Production Office ESTEC, 2009. Available from: <http://sci.esa.int/science-e/www/object/index.cfm?fobjectid=47218>. ISBN 978-92-9221-975-8.
- [24] GURNETT, D. a. et al. Radar soundings of the ionosphere of Mars. *Science (New York, N.Y.)*. December 2005, 310, 5756, pages 1929–33. ISSN 1095-9203. doi: 10.1126/science.1121868. Available from: <http://www.ncbi.nlm.nih.gov/pubmed/16319123>.
- [25] JAUMANN, R. et al. The high-resolution stereo camera (HRSC) experiment on Mars Express: Instrument aspects and experiment conduct from interplanetary cruise through the nominal mission. *Planetary and Space Science*. May 2007, 55, 7-8, pages 928–952. ISSN 00320633. doi: 10.1016/j.pss.2006.12.003. Available from: <http://linkinghub.elsevier.com/retrieve/pii/S0032063306003448>.
- [26] JAVA.NET. *JAXB Reference Implementation*. In *Project JAXB* [online], 2013. [Accessed 04/08/2013]. Available from: <http://jaxb.java.net/>.
- [27] JPL. *Planetary Data System Standards Reference*. Jet Propulsion Laboratory, California Institute of Technology, Pasadena, California, 2009. Available from: <http://pds.nasa.gov/tools/standards-reference.shtml>.

- [28] LOIZEAU, D. et al. Characterization of hydrated silicate-bearing outcrops in Tyrrhena Terra, Mars: Implications to the alteration history of Mars. *Icarus*. May 2012, 219, 1, pages 476–497. ISSN 00191035. doi: 10.1016/j.icarus.2012.03.017. Available from: <http://linkinghub.elsevier.com/retrieve/pii/S0019103512001108>.
- [29] MALTAGLIATI, L. et al. Evidence of water vapor in excess of saturation in the atmosphere of Mars. *Science (New York, N.Y.)*. September 2011, 333, 6051, pages 1868–71. ISSN 1095-9203. doi: 10.1126/science.1207957. Available from: <http://www.ncbi.nlm.nih.gov/pubmed/21960630>.
- [30] MANGOLD, N. et al. Geomorphic study of fluvial landforms on the northern Valles Marineris plateau, Mars. *Journal of Geophysical Research*. August 2008, 113, E8, pages E08009. ISSN 0148-0227. doi: 10.1029/2007JE002985. Available from: <http://www.agu.org/pubs/crossref/2008/2007JE002985.shtml>.
- [31] MARQUARDT, D. W. An Algorithm for Least-Squares Estimation of Nonlinear Parameters. *Journal of the Society for Industrial and Applied Mathematics*. June 1963, 11, 2, pages 431–441. ISSN 0368-4245. doi: 10.1137/0111030. Available from: <http://pubs.siam.org/doi/abs/10.1137/0111030>.
- [32] MASSÉ, M. et al. Mineralogical composition, structure, morphology, and geological history of Aram Chaos crater fill on Mars derived from OMEGA Mars Express data. *Journal of Geophysical Research*. December 2008, 113, E12, pages E12006. ISSN 0148-0227. doi: 10.1029/2008JE003131. Available from: <http://www.agu.org/pubs/crossref/2008/2008JE003131.shtml>.
- [33] MONTMESSIN, F. et al. Hyperspectral imaging of convective CO<sub>2</sub> ice clouds in the equatorial mesosphere of Mars. *Journal of Geophysical Research*. November 2007, 112, E11, pages E11S90. ISSN 0148-0227. doi: 10.1029/2007JE002944. Available from: <http://www.agu.org/pubs/crossref/2007/2007JE002944.shtml>.
- [34] NEUKUM, G. *Amenthes Planum topography*. In *Space In Images* [online], 2013. [Accessed 03/21/2013]. Available from: [http://spaceinimages.esa.int/Images/2013/02/Amenthes\\_Planum\\_topography](http://spaceinimages.esa.int/Images/2013/02/Amenthes_Planum_topography).
- [35] PERRIER, S. et al. Global distribution of total ozone on Mars from SPICAM/MEX UV measurements. *Journal of Geophysical Research*. 2006, 111, E9, pages E09S06. ISSN 0148-0227. doi: 10.1029/2006JE002681. Available from: <http://www.agu.org/pubs/crossref/2006/2006JE002681.shtml>.

- [36] PHILLIPS, R. J. et al. Mars north polar deposits: stratigraphy, age, and geodynamical response. *Science (New York, N.Y.)*. May 2008, 320, 5880, pages 1182–5. ISSN 1095-9203. doi: 10.1126/science.1157546. Available from: <http://www.ncbi.nlm.nih.gov/pubmed/18483402>.
- [37] SCARGLE, J. Studies in astronomical time series analysis. II-Statistical aspects of spectral analysis of unevenly spaced data. *The Astrophysical Journal*. 1982, 263, pages 835–853. Available from: <http://articles.adsabs.harvard.edu/full/1982ApJ...263..835S>.

# List of Tables

# List of Abbreviations

# Attachments

## Active Ionospheric Sounding data format

Listing 3.1: Active Ionospheric Sounding data format

```
1 OBJECT = COLUMN
  NAME = SCLK_SECOND
3  DATA_TYPE = MSB_UNSIGNED_INTEGER
  START_BYTE = 1
5  BYTES = 4
  DESCRIPTION = "Spacecraft clock counter of onboard seconds,
7                           since the epoch of May 3, 2003 (123)."
  END_OBJECT = COLUMN
9
10 OBJECT = COLUMN
11  NAME = SCLK_PARTITION
12  DATA_TYPE = MSB_UNSIGNED_INTEGER
13  START_BYTE = 5
14  BYTES = 2
15  DESCRIPTION = "Spacecraft clock counter partition of onboard
                           counter roll-over/reset. Zero or one
16                           indicates the counter is in the first
17                           partition. See the NAIF Spice documentation."
18  END_OBJECT = COLUMN
19
20 OBJECT = COLUMN
21  NAME = SCLK_FINE
22  DATA_TYPE = MSB_UNSIGNED_INTEGER
23  START_BYTE = 7
24  BYTES = 2
25  DESCRIPTION = "Spacecraft clock counter of onboard fractions
                           of a second with one fraction being 1/65536."
26  END_OBJECT = COLUMN
27
28 OBJECT = COLUMN
29  NAME = SCET_DAYS
30  DATA_TYPE = MSB_UNSIGNED_INTEGER
31  START_BYTE = 9
32  BYTES = 4
33  DESCRIPTION = "Spacecraft event time in days since
                           1958-001T00:00:00Z. This is the historical
34                           epoch used since the launch of the first U.S.
35                           satellite Explorer I with Dr. James Van Allen's
36                           (University of Iowa) cosmic-ray instrument as
37                           the principal element of the payload, resulting
38                           in the discovery of the Van Allen Radiation
39                           Belts."
40
41  END_OBJECT = COLUMN
42
43 OBJECT = COLUMN
44  NAME = SCET_MSEC
45  DATA_TYPE = MSB_UNSIGNED_INTEGER
46  START_BYTE = 13
47  BYTES = 4
48  DESCRIPTION = "Spacecraft event time in milliseconds of day.
49                           SCET_DAYS and SCET_MSEC are provided to
50                           accurately time tag the data in UTC without
```

```

53                         the need for calls to the spice kernel."
END_OBJECT = COLUMN
55
OBJECT = COLUMN
57   NAME = SCET_STRING
DATA_TYPE = CHARACTER
59   START_BYTE = 25
BYTES = 24
61   DESCRIPTION = "Spacecraft event time in UTC in human readable
                  ASCII format."
63 END_OBJECT = COLUMN

65 OBJECT = COLUMN
NAME = PROCESS_ID
67 DATA_TYPE = MSB_UNSIGNED_INTEGER
START_BYTE = 49
69 BYTES = 1
DESCRIPTION = "The seven bits from the 20,3 telemetry packet
                  header which determine the instrument process id.
                  0x4D (77d) = Subsurface Sounder (SS1 to SS4)
                  0x4E (78d) = Active Ionospheric Sounder (AIS)
                  0x4F (79d) = Calibration (CAL)
                  0x50 (80d) = Receive Only (RCV)"
71
73
75
77
OBJECT = COLUMN
79   NAME = INSTRUMENT_MODE
DATA_TYPE = MSB_UNSIGNED_INTEGER
81   START_BYTE = 50
BYTES = 1
83   DESCRIPTION = "The bits from the 20,3 telemetry packet header
                  used to determine the instrument data type and
                  mode selection."
85
87   OBJECT = BIT_COLUMN
NAME = DATA_TYPE
BIT_DATA_TYPE = MSB_UNSIGNED_INTEGER
89   START_BIT = 1
BITS = 4
91   DESCRIPTION = " 0001 = AIS, Calibration, or Receive Only
                  0000 = SS1-SS5 Individual Echoes
                  0010 = SS1-SS5 Acquisition
                  0011 = SS1-SS5 Tracking "
93
95   END_OBJECT = BIT_COLUMN
OBJECT = BIT_COLUMN
97   NAME = MODE_SELECTION
BIT_DATA_TYPE = MSB_UNSIGNED_INTEGER
99   START_BIT = 5
BITS = 4
101  DESCRIPTION = " 0101 = Calibration
                  0110 = Receive Only
                  0111 = Active Ionospheric Sounder
                  1000 = Subsurface Sounder 1
103
105
107
109  END_OBJECT = BIT_COLUMN
END_OBJECT = COLUMN
111
OBJECT = COLUMN
113   NAME = TRANSMIT_POWER

```

```

        DATA_TYPE = MSB_UNSIGNED_INTEGER
115    START_BYTE = 60
        BYTES = 1
117    DESCRIPTION = "The transmit power level, expressed as the
                      power supply regulation voltage for the
119          final power amplifier output.
120          0x00 (0d) = minimum transmit power 2.5V
121          0x0F (15d) = maximum transmit power 40.0V "
122    END_OBJECT = COLUMN
123
        OBJECT = COLUMN
125    NAME = FREQUENCY_TABLE_NUMBER
        DATA_TYPE = MSB_UNSIGNED_INTEGER
127    START_BYTE = 61
        BYTES = 1
129    DESCRIPTION = "The Active Ionospheric Sounder may select
                      one of sixteen frequency tables to use during
131          transmit. Each table has 160 frequencies
                      that are transmitted during an AIS capture.
132          Table 0 is the default table."
133    END_OBJECT = COLUMN
134
        OBJECT = COLUMN
136    NAME = FREQUENCY_NUMBER
        DATA_TYPE = MSB_UNSIGNED_INTEGER
138    START_BYTE = 62
        BYTES = 1
140    DESCRIPTION = "The frequency number from the table, ranging
                      from 0 to 159."
142    END_OBJECT = COLUMN
143
        OBJECT = COLUMN
145    NAME = BAND_NUMBER
        DATA_TYPE = MSB_UNSIGNED_INTEGER
147    START_BYTE = 63
        BYTES = 1
149    DESCRIPTION = "The band that was selected to receive the echo.
150          0 = band 0 3 = band 3
151          1 = band 1 4 = band 4
152          2 = band 2"
153    END_OBJECT = COLUMN
154
        OBJECT = COLUMN
156    NAME = RECEIVER_ATTENUATION
        DATA_TYPE = MSB_UNSIGNED_INTEGER
158    START_BYTE = 64
        BYTES = 1
160    DESCRIPTION = "The receiver attenuation for band selected
                      measured in dB."
162    END_OBJECT = COLUMN
163
        OBJECT = COLUMN
165    NAME = FREQUENCY
        DATA_TYPE = IEEE_REAL
167    START_BYTE = 77
        BYTES = 4
        UNIT = HZ
169    DESCRIPTION = "The frequency of the transmit pulse"
170    END_OBJECT = COLUMN
171
        OBJECT = COLUMN

```

```

175  NAME = SPECTRAL_DENSITY
176  DATA_TYPE = IEEE_REAL
177  START_BYTE = 81
178  BYTES = 320
179  ITEMS = 80
180  ITEM_BYTES = 4
181  UNIT = "VOLT**2/M**2/HZ"
182  DESCRIPTION = "A series of calibrated spectral densities
183          from a single transmit pulse,"
184  END_OBJECT = COLUMN

```

## Result file format

Listing 3.2: The XML Schema of the results file

```

<?xml version="1.0" encoding="UTF-8"?>
2 <schema xmlns="http://www.w3.org/2001/XMLSchema" targetNamespace="http://www.mff.cuni.cz/~peckam/
  java/ais-detection-result"
  xmlns:tns="http://www.mff.cuni.cz/~peckam/java/ais-detection-result"
4   xmlns:jxb="http://java.sun.com/xml/ns/jaxb"
  xmlns:xjc="http://java.sun.com/xml/ns/jaxb/xjc"
6   jxb:extensionBindingPrefixes="xjc"
  elementFormDefault="qualified"
8   jxb:version="1.0">

10  <annotation>
11    <appinfo>
12      <jxb:schemaBindings>
13        <jxb:package name="cz.cuni.mff.peckam.ais.result"></jxb:package>
14      </jxb:schemaBindings>
15      <jxb:globalBindings>
16        <xjc:simple/>
17        <jxb:javaType name="Float" xmlType="float"
18          parseMethod="javax.xml.bind.DatatypeConverter.parseFloat"
19          printMethod="cz.cuni.mff.peckam.ais.result.JAXBValueConverter
20            .printFloatThreeDecimals"/>
21      </jxb:globalBindings>
22    </appinfo>
23  </annotation>

24  <element name="orbit" type="tns:orbitType"></element>

26  <complexType name="orbitType">
27    <sequence maxOccurs="unbounded" minOccurs="1">
28      <element name="frame" type="tns:frameType"></element>
29    </sequence>
30    <attribute name="id" type="int" use="required"></attribute>
31  </complexType>

32  <complexType name="frameType">
33    <sequence>
34      <element name="time" type="tns:datetime"></element>
35      <element name="sza" type="float" minOccurs="0"></element>
36      <element name="alt" type="int" minOccurs="0"></element>
37      <element name="lat" type="float" minOccurs="0"></element>
38      <element name="lon" type="float" minOccurs="0"></element>
39      <element name="x" type="float" minOccurs="0"></element>
40      <element name="rho" type="float" minOccurs="0"></element>
41      <element name="hperiod" type="float" minOccurs="0"></element>

```

```

        <element name="hperiodquality" type="tns:boolAsInt" minOccurs="0"></element>
    >
44        <element name="vperiod" type="float" minOccurs="0"></element>
45        <element name="cutoff" type="float" minOccurs="0"></element>
46        <element name="ionospheretrace" type="tns:traceType" minOccurs="0"></element>
47        <element name="groundtrace" type="tns:traceType" minOccurs="0"></element>
48    </sequence>
49 </complexType>
50
51 <complexType name="traceType">
52     <sequence>
53         <element name="point" type="tns:pointType" maxOccurs="unbounded" minOccurs="1"></
54             element>
55     </sequence>
56 </complexType>
57
58 <complexType name="pointType">
59     <attribute name="x" type="float" use="required"></attribute>
60     <attribute name="y" type="float" use="required"></attribute>
61 </complexType>
62
63     <simpleType name="datetime">
64         <annotation>
65             <appinfo>
66                 <jxb:javaType name="org.joda.time.DateTime"
67                     parseMethod="org.joda.time.DateTime.parse"
68                     printMethod="cz.cuni.mff.peckam.ais.result.JAXBValueConverter
69                     .printDateTime"/>
70             </appinfo>
71         </annotation>
72         <restriction base="string"/>
73     </simpleType>
74
75     <simpleType name="boolAsInt">
76         <restriction base="int">
77             <minInclusive value="0"/>
78             <maxInclusive value="1"/>
79         </restriction>
80     </simpleType>
81 </schema>

```